American Mineralogist, Volume 91, pages 589–603, 2006

Cation redistribution in the octahedral sheet during diagenesis of illite-smectites from Jurassic and Cambrian oil source rock shales

LIDIA G. DAINYAK,[1] VICTOR A. DRITS,[1] BELLA B. ZVIAGINA,[1] AND HOLGER LINDGREEN[2,*]

[1]Geological Institute, Russian Academy of Science, Pyzhevsky per. D7, 109017 Moscow, Russia
[2]Clay Mineralogical Laboratory, Geological Survey of Denmark and Greenland, Øster Voldgade 10, DK–1350 Copenhagen K, Denmark

ABSTRACT

During diagenesis of Jurassic and Cambrian oil source rock shales illite-smectite(-vermiculite) [I-S(-V)] is transformed to illite-tobelite-smectite(-vermiculite) [I-T-S(-V)]. This transformation of S layers to T layers takes place by an increase in tetrahedral charge through Al for Si substitution and subsequent fixation of interlayer NH_4, accompanied by an increase in Al and a decrease in Fe and Mg in the octahedral sheet. In the present investigation, the distribution of isomorphous cations in octahedral sheets of trans-vacant I-S(-V) and I-T-S(-V) was studied by Mössbauer and Infrared (IR) spectroscopies. Mössbauer spectra have been modeled using numerical values of the Fe^{3+} and Fe^{2+} quadrupole doublets corresponding to local cation arrangements around Fe^{3+} and Fe^{2+} in octahedral sheets of micaceous minerals. To interpret IR spectra in the OH-stretching region, frequencies for each pair of cations bonded to OH groups determined for micas and I-S are used. Combination of Mössbauer and IR data by computer simulation provides two-dimensional cation distributions of octahedral cations. The Jurassic and Cambrian I-S(-V) and I-T-S(-V) have clustered octahedral sheets. Ordered clusters of mixed cation composition (Mg, Al, Fe^{3+}, and Fe^{2+}) with regular alternation of di- and trivalent cations and Fe^{3+}-clusters dispersed over an Al-matrix are found in detrital samples. In diagenetically transformed samples, ordered clusters persist while Fe^{3+}-clusters degenerate to either short chains consisting of two Fe-Fe pairs or to isolated Fe-Fe pairs oriented along the $\boldsymbol{b}$, $\boldsymbol{b_1}$, and $\boldsymbol{b_2}$ directions. The release of Fe and Mg during diagenesis occurs from Fe^{3+} clusters and through partial destruction of ordered clusters and of $\boldsymbol{b_1}$, $\boldsymbol{b_2}$-oriented Mg-Mg pairs. However, as the cation composition and the short-range cation order within the clusters are preserved and the Al for Fe and Mg substitution occurs at cluster edges, the diagenetic transformation of S (and V) to T layers in both the Jurassic and Cambrian I-S(-V) proceeds through a solid-phase transformation and not through dissolution-reprecipitation.

Keywords: Illite-smectite, cation distribution, computer simulation

INTRODUCTION

Mixed-layer illite-smectite (I-S) is a typical component of, e.g., shales, K-bentonites, mudstones, and hydrothermally altered rocks. Transformation of smectite into illite through a series of I-S is accompanied by increasing of illite interlayers, and a tendency to ordering in the distribution of illite and smectite interlayers (e.g., Shutov et al. 1969a, 1969b; Perry and Hower 1970; Hower et al. 1976). The increase in illite layers in I-S occurs by tetrahedral Al for Si substitution and replacement of exchangeable cations by fixed K and/or NH_4 (Hower et al. 1976; Lindgreen et al. 1991, 2000; Lindgreen 1994; Drits et al. 2002). In the octahedral sheets of the interstratified layers, this reaction includes an increase in Al and $Fe^{2+}/(Fe^{2+}+Fe^{3+})$ and a decrease in Mg and Fe (Eslinger et al. 1979; Nadeau and Bain 1986; Lindgreen et al. 1991, 2000; Środoń et al. 1992; Cuadros and Altaner 1998; Drits et al. 2002). Therefore, diagenetic changes in the cation distribution of the octahedral sheets in I-S are important to understand the mechanism of smectite illitization.

Determination of the actual cation distributions in dioctahedral 2:1 phyllosilicates and especially in I-S have been performed, most of them recently (Dainyak et al. 1992; Drits et al. 1997a; Muller et al. 1997; Cuadros et al. 1999; Manceau et al. 2001; Sainz-Diaz et al. 2001a, 2001b, 2002, 2003a, 2003b; Timon et al. 2003). Assignment of Fe^{3+} to *trans*- and *cis*-sites based on Mössbauer spectroscopy alone was replaced by a long-range distribution of octahedral cations over *cis*- and *trans*-sites determined by diffraction methods (Bookin et al. 1978; Dainyak et al. 1981; Dainyak and Drits 1987; Dainyak et al. 1992). In particular, the observed differences in the quadrupole splittings of Fe^{3+} cations are assumed to be due to distortions of Fe^{3+} octahedra by different local cation environments. Quadrupole splittings for each local cation environment have been deduced for Fe^{3+} (Drits et al. 1997a; Dainyak and Kheifits 1999) and, recently, for Fe^{2+} based on relationships between the quadrupole splitting and the corresponding local cation arrangements around these cations (Dainyak et al. 2004). These assignments allow presenting the fitted broadened doublets as groups of closely overlapping peaks. Similar presentation of the fitted doublets follows from quadrupole splitting distribution (QSD) analysis (Wivel and Mørup 1981; Rancourt and Ping 1991; Rusakov 1999). It was pointed out (Rancourt 1994) that two discrete doublets in the spectra of trioctahedral biotite and annite cannot be assigned to *cis*- and *trans*-sites and should be replaced by a QSD because the local structural disorder due to cation distribution does influences the Fe^{2+} Mössbauer parameters independent of the structural location

* E-mail: hl@geus.dk

of this cation. These effects were demonstrated in a spectrum for synthetic fluorannite where several distinct local environment contributions were resolved (Rancourt et al. 1996). However, Shabani et al. (1998), based on two main QSD components, found the Fe^{2+} populations in *cis*- and *trans*-sites in non-stoichiometric muscovites, in which the sum of octahedral cations per formula unit is greater than that for muscovite of idealized composition.

An effective way to determine cation distributions is by the combination of diffraction and spectroscopic techniques. The method for determination of order-disorder in cation distribution as proposed by Dainyak et al. (1992, 1999, 2004), Cuadros et al. (1999) and Sainz-Diaz et al. (2001a, 2001b, 2002, 2003a, 2003b) is based on computer simulation of the two-dimensional distribution of isomorphous cations in the octahedral sheets of dioctahedral 2:1 layers that satisfies equally well the experimental data obtained by Mössbauer and Infrared (IR) spectroscopies. In particular, the reliable interpretation of IR spectra of dioctahedral mica-like and smectite minerals in the OH-stretching vibration region (Besson and Drits 1997a, 1997b; Zviagina et al. 2002, 2004) provides data on the occurrence probabilities for various types of OH-linked cation pairs.

Dainyak et al. (1992) used IR and Mössbauer techniques in combination with computer simulation and showed that one glauconite, sample B. Patom, is composed of small illite-like and celadonite-like clusters. Similar distributions were found for Fe^{3+}-bearing micas by a combination of X-ray diffraction (XRD), extended X-ray absorption fine structure (EXAFS) analysis, IR, Mössbauer spectroscopy, and computer simulation (Drits et al. 1997a). Muller et al. (1997) showed using XRD, EXAFS, and IR that Fe and Mg are segregated in small clusters in the Al-rich octahedral sheets of the montmorillonite from Camp-Bertaux. Cuadros et al. (1999), Sainz-Diaz et al. (2001a, 2001b, 2002, 2003a, 2003b), and Timon et al. (2003) studied the cation distribution in the octahedral sheets of I-S from bentonite using ^{27}Al nuclear magnetic resonance (NMR), IR, and inverse Monte Carlo simulation techniques. They found that Fe cations have a tendency to be segregated and that Fe segregation increases with the proportion of illite, whereas Mg cations are dispersed among other cations.

The I-S in oil source shales from the Jurassic of the North Sea and the Cambrian from the Baltic region were studied previously. During diagenesis and oil formation, smectite layers are transformed into NH_4^+-bearing illite (tobelite) layers by a solid-state tetrahedral Al for Si substitution and an interlayer fixation of NH_4^+ released from organic matter during oil generation (Lindgreen 1994; Drits et al. 1997b, 2002; Lindgreen et al. 2000). The aim of the present work is, first, to use Mössbauer and IR spectroscopies and computer simulation to reconstruct cation distribution in octahedral sheets of I-S from shales and, second, to analyze the dynamics of octahedral cation redistribution during diagenetic transformation of these I-S.

Samples and experiments

Samples

The Upper Jurassic shale samples investigated were core material from the E1 well, 2984 m depth (sample 112), the S.E. Igor well, 2502 m depth (X3), the N. Jens 1 well, 2965 m (X6), and Elin the 1 well, 4418 m (X18), and cuttings material from the 2/7-3 well, 3789 m depth (sample 89), the 2/11–1 well, 4548 m depth (sample 87), and the U1 well, 2899 m depth (sample 82).

The Cambrian samples investigated were outcrop material from Aakarpsmölle, Scania (sample AA), Bornholm, Denmark (sample OL), Estonia (sample ES), N. Nærnæs, Norway (OS), and core samples from well Slagelse 1, 2933 m (sample SL).

Sample pretreatment

The samples were dispersed ultrasonically and pretreated for removal of organic matter with NaOCl (Anderson 1963) and of Fe and Al oxides by the dithionite-citrate method (Mehra and Jackson 1960). A fine clay fraction was isolated by centrifugation (Hansen and Lindgreen 1989), and this fraction is dominated by mixed-layer I-S-V along with kaolinite.

Structural and chemical features of the studied I-S

The formation of NH_4-bearing illite (tobelite) during diagenesis is the main process in the Jurassic and Cambrian oil source rocks (Drits et al. 1997b, 2002; Lindgreen et al. 2000). The charge of the octahedral sheet decreases by release of Mg and the incorporation of Al whereas the release of Fe^{3+} does not affect the charge.

The structural formulae of the samples (Drits et al. 1997b, 2002; Lindgreen et al. 2000) are shown in Table 1. During diagenesis in the Upper Jurassic North Sea samples, I-S-V having ~65% I layers and 8% T layers and tendency to layer segregation are transformed to I-T-S-V having ~65% I and ~20% T layers and maximum ordering of the I + T and S layers for Reichweite (R) = 1. Diagenesis in the Baltic Cambrian shale transforms I-S having ~75% I layers to I-T-S having ~80% I layers and ~15% T layers. All the Upper Jurassic samples except X18 contain kaolinite (2–11%). The crystal-chemical formulae of the I-T-S-V component in these kaolinite-bearing samples were calculated using bulk-chemical analyses and NMR data as described in Drits et al. (2002). Table 1 shows that the diagenetic transformation of the North Sea samples is accompanied by a significant increase in the amounts of fixed interlayer NH_4 and of ^{VI}Al. The octahedral cation composition of the 2:1 layers also changes: the ^{VI}Al increases from 1.42 to 1.69 cations per $O_{10}(OH)_2$, whereas the Fe and Mg contents decrease from 0.29 to 0.15 and from 0.37 to 0.14, respectively. All the samples consist of *trans*-vacant 2:1 layers. The samples from the Baltic region show the same regularities in the variation of the cation composition, i.e., an increase in ^{IV}Al, NH_4, and ^{VI}Al and a decrease in Fe and Mg (Table 1).

Mössbauer spectroscopy

Mössbauer spectra were measured at ambient temperature (RT) on a spectrometer with a constant acceleration drive using a ^{57}Co (Rh) source (experimental half-width Γ = 0.23 mm/s with a thin Fe foil). All spectra were calibrated with reference to α-Fe. To eliminate orientation effects, the absorber was at an angle of 54.7° to the radiation. The absorber thickness was <3 mg Fe/cm^2 with the absorber in the inclined position.

The spectra were computer-fitted using a least-squares iterative procedure with doublets having equal intensities and halfwidths and Lorentzian shapes (Dainyak 1980). The initial number of doublets used in fits was determined by visual inspection, taking account of spectral features. As the fitting of Mössbauer spectra is not a precise mathematical problem, the final number of fitted doublets was chosen not only by the acceptability of χ^2 values, but by also including the distances between components in the fitted spectra and any unjustifiable broadening of the peaks. The doublets for tetrahedral Fe^{3+} were not included in the fitting procedure because, according to the IR spectra, the samples contain no tetrahedral Fe^{3+}.

IR spectroscopy

The IR spectra were recorded on a Nicolet ESP-260 FTIR spectrometer within the 300–4000 cm^{-1} range, with a 4 cm^{-1} resolution. Background correction and IR absorbance conversion were made automatically with the Nicolet Omnic software version 5.0.

A special sample-preparation procedure was used to remove most of the molecular H_2O from the smectite samples (McCarty et al. 2004). The material was oven-dried, then freeze-dried, homogenized with KBr, placed into a pellet die, and pressed under vacuum. The pellet was placed into a vacuum oven and heated at 185 °C for at least 14 h and then cooled for 30 min in a dessicant box.

The OH-stretching regions of the spectra (3200–3750 cm^{-1}) were decomposed and fitted using the Galactic PeakSolve program assuming a symmetric Gaussian peak shape for each OH band. The variable parameters were position, width at half-height, and intensity of each component. The quality of spectral decomposition

TABLE 1. Structural formulae for the I-S-V and I-T-S-V [per $O_{10}(OH)_2$] and mean percentages for the S, I, and T components (Drits et al. 1997 and Lindgreen et al. 2000)

Sample	Si	^{IV}Al	^{VI}Al	Fe^{3+}	Fe^{2+}	Mg	K	NH_4	Ca	Na	Mg	S+V	I	T
Jurassic series														
X3	3.63	0.37	1.42	0.19	0.03	0.37	0.38	0.07	–	0.25	–	25	67	8
82	3.67	0.33	1.63	0.23	0.05	0.30	0.36	0.08	0.01	0.24	–	27	66	7
X6	3.48	0.52	1.46	0.17	0.06	0.31	0.39	0.23	0.03	0.21	–	17	63	20
87	3.45	0.55	1.51	0.22	0.07	0.20	0.38	0.16	0.02	0.23	–	20	64	16
89	3.35	0.65	1.69	0.12	0.04	0.14	0.40	0.22	0.03	0.15	–	16	65	19
X18	3.39	0.61	1.63	0.09	0.06	0.22	0.55	0.19	–	0.16	–	10	71	19
Cambrian series												S	I	T
ES	3.55	0.45	1.49	0.18	0.06	0.27	0.55	0.02	–	0.02	0.05	25	75	–
OL	3.37	0.63	1.71	0.05	0.02	0.22	0.57	0.15	–	0.02	–	10	75	15
AA	3.34	0.66	1.72	0.05	0.02	0.21	0.50	0.17	–	0.02	0.03	10	72	18
OS	3.36	0.64	1.69	0.03	0.03	0.25	0.55	0.13	0.01	0.02	0.05	4	84	12
SL	3.35	0.65	1.73	0.04	0.04	0.19	0.56	0.09	–	0.01	0.05	4	84	12

Note: The samples are listed according to increasing degree of transformation.

was estimated by the minimization function, χ^2, and the correlation coefficient, R, as well as by the agreement between the experimental spectrum profile with that synthesized by summation of the extracted individual bands. The integrated optical densities were assumed to be proportional to the areas of the corresponding peaks, with equal absorption coefficients for all types of OH-bonded cation pairs.

INTERPRETATION

Mössbauer spectra of *trans*-vacant 2:1 phyllosilicates

According to X-ray and electron diffraction, Fe-illites, glauconites, celadonites, leucophyllites, and nontronites consist of *trans*-vacant (*tv*) 2:1 layers (Tsipursky et al. 1978; Sakharov et al. 1990; Besson et al. 1983; Manceau et al. 2001; Cuadros 2002). As Fe^{3+} cations occupy only octahedral *cis*-sites, the number of fitted doublets is expected to be due to specific local cationic arrangements around Fe^{3+}. For the four types of octahedral cations (Al, Fe^{3+}, Fe^{2+}, and Mg), there are 20 local cation arrangements ($3Fe^{3+}$, 3Al, $2AlFe^{3+}$, etc.; see Table 2). The corresponding individual doublets are not resolved in the Mössbauer spectra because of small differences in their spectral parameters compared to the line width. Thus, the spectra consist of groups of closely overlapping peaks, from which statistically acceptable fits usually can be obtained with two to four broadened Lorentzian doublets for Fe^{3+} and with two or three doublets for Fe^{2+}. With thin absorbers and assuming the same recoil-free fraction values for Fe in different local arrangements, each of these "experimental" j doublets may be composed of individual doublets with a small range of quadrupole splittings, Δ_i, each Δ_i corresponding to a definite local cationic arrangement with the occurrence probability w_i.

The electric field gradient (EFG) on Fe^{3+} is largely due to lattice contributions, q_{lat}, and depends mainly on distortion of Fe^{3+} octahedra: the more distortion, the greater the EFG (see e.g., Bancroft 1974; Goodman 1976; Coey 1980). This is assumed in the empirical equation of Drits et al. (1997a) where the Δ_i^{pred} values are calculated by incorporating the charge, Z^{av}, and bond length, d^{av}, averaged over three charges and three mean bond lengths, respectively, in the three octahedra nearest to Fe^{3+}. The mean M-O, OH bond lengths for Fe^{3+}-, Fe^{2+}-, Mg-, and Al-octahedra in dioctahedral 2:1 layer silicates are given by Drits (1975) and Smoliar-Zviagina (1993). Table 2 shows individual Δ_i^{pred} values for the local cationic arrangements.

The interpretation of quadrupole splittings for Fe^{2+} doublets is more difficult because of the main valence contribution, q_{val}, to the EFG. For micaceous minerals, Dainyak et al. (2004) found correlations between Δ_j^{fit} of Fe^{2+} derived from computer fits of the corresponding spectra and the cation compositions of local cation arrangements around Fe^{2+} having occurrence probabilities w_i. From these correlations, individual tentative quadrupole splittings, Δ_i^{tent}, were derived for Fe^{2+}. The order of local cation arrangements with respect to increasing quadrupole splitting was found to be the same both for Fe^{3+} and Fe^{2+}. This relationship implies a direct dependence of the Fe^{2+} quadrupole splitting on the structural distortion at the Fe^{2+} site. The Δ_i^{tent} values for Fe^{2+} are shown in Table 2.

Using the predicted Δ_i^{pred} values for Fe^{3+} and the tentative Δ_i^{tent} for Fe^{2+}, the "fine structure" of the j doublets Fe^{3+} and Fe^{2+} fitted to the spectrum is assumed to be solved when the modeled two-dimensional cation distribution results in satisfactory fits for the relative areas S_j and the Δ_j values for the Fe^{3+} and Fe^{2+} doublets.

Interpretation of IR spectra in the OH-stretching region

In the present work, the assignment of the individual OH-stretching bands corresponding to specific types of OH-bonded cation pairs follows, in general, the band attributions suggested by Besson and Drits (1997a, 1997b) for dioctahedral micas. The positions of the individual bands in the spectra of dioctahedral smectites are known to differ from those in the spectra of dioctahedral micas (Zviagina et al. 2004). However, for I-S with prevalent mica-like interlayers, the band attributions found for micas are relevant. Therefore, the use of the band assignments suggested for dioctahedral micas for the interpretation of the OH-stretching regions of the IR spectra of mixed-layer I-S and I-T-S was justified by the relatively low proportions of expandable layers (16–27% in the Upper Jurassic series, Drits et al. 2002); 18% in ES and 4–10% in the other samples from the Cambrian series (Lindgreen et al. 2000) and the high number of fixed K and NH_4^+ cations in the samples (Table 1).

In accordance with Besson and Drits (1997a, 1997b), the complex wide absorption band of the residual H_2O was included in the fitted spectrum as two broad maxima around 3200 and 3420 cm^{-1}.

All the spectra, except that of ES, contained a broad pronounced band at about 3305–3313 cm^{-1}, which was attributed to the stretching vibration of ammonium, as all these samples contained fixed NH_4 (Table 1).

TABLE 2. Mössbauer spectroscopy of sample X3 showing the local cationic arrangements in order of increasing individual Δ_i^{pred} values

Arrangement	Fe^{3+}				Fe^{2+}			
	Δ_i^{pred}, mm/s	w_i	w_i^n	$\Delta_i^{pred}w_i^n$	Δ_i^{tent}, mm/s	w_i	w_i^n	$\Delta_i^{tent}w_i^n$
$3Fe^{2+}$	0.				1.20			
$2Fe^{2+}Mg$	0.13	0.005	0.016	0.002	1.40			
$3Fe^{3+}$	0.17	0.009	0.029	0.005	**1.61**	0.020	0.067	0.107
$2MgFe^{2+}$	0.26	0.055	0.176	0.046	**1.70**			
$2Fe^{3+}Al$	0.33	0.241	0.770	0.254	**1.85**	0.075	0.250	0.462
$2Fe^{2+}Fe^{3+}$	0.34	0.003	0.009	0.003	1.87			
$3Mg$	0.39	0.011	0.020	0.008	**1.90**			
$MgFe^{2+}Fe^{3+}$	0.48	0.004	0.007	0.003	2.10			
$2Fe^{2+}Al$	0.49				2.30			
$2AlFe^{3+}$	0.51	0.145	0.269	0.137	**2.49**	0.205	0.683	1.701
$2MgFe^{3+}$	0.61	0.025	0.046	0.028	2.60			
$AlMgFe^{2+}$	0.63	0.015	0.028	0.017	2.66			
$2Fe^{3+}Fe^{2+}$	0.65				2.75			
$3Al$	0.74	0.245	0.455	0.337	**2.84**	0.67	0.957	2.718
$2MgAl$	0.78	0.080	0.149	0.116	**2.85**			
$2Fe^{3+}Mg$	0.79	0.003	0.005	0.004	**2.87**			
$AlFe^{2+}Fe^{3+}$	0.86	0.010	0.018	0.016	2.87			
$AlMgFe^{3+}$	1.02	0.071	0.473	0.483	2.87	0.030	0.043	0.123
$2AlFe^{2+}$	1.06	0.019	0.126	0.134	2.90			
$2AlMg$	1.40	0.060	0.400	0.560	**2.96**			
Δ_j^{calc}(mm/s)=$\Sigma_i\Delta_i^{pred}w_i^n$	A 0.31		D	2.27	Δ_j^{tent}(mm/s)=$\Sigma_i\Delta_i^{tent}w_i^n$			
	B 0.65							
	C 1.18							
			E	2.84				

Notes: Calculation of the Δ_j^{calc} values for Fe^{3+} (A, B, C) and Fe^{2+} (D, E) doublets fitted to the spectrum. The grouping controlled by function F in the simulation procedure is indicated by underlines.

Simulation of two-dimensional octahedral cation distributions to satisfy the parameters fitted to Mössbauer spectra

The improved version of the program for simulating two-dimensional octahedral cation distributions (Dainyak et al. 2004) and previous versions (Dainyak et al. 1992; Dainyak and Kheifits 1999; Drits et al. 2002) incorporate integrated IR optical densities for bands, W_{ik}, where i and k are the cations (Al, Fe^{3+}, Fe^{2+}, and Mg) bound to the OH groups (Slonimskaya et al. 1986; Besson and Drits 1997a, 1997b; Madejova et al. 1992, 1994). Because the W_{ik} values are proportional to the sum of occurrence probabilities, w_{ik} and w_{ki}, one cation may equally well occupy the M2 and M2' (Fig. 1) *cis*-sites or preferentially one of these sites. For example, if W_{AlMg} is 0.3 and Mg prefers the M2' site, then we have $w_{AlMg} = 0.3$ and $w_{MgAl} = 0$.

Because the direction of adjacent occupied octahedra in *tv* 2:1 layers coincides with the ***b*** axis, the corresponding cation pairs can be referred to as ***b***-oriented. The simulation program uses a heuristic algorithm consisting of two stages. The first stage is random filling of the honeycomb pattern of the dioctahedral sheet having ***b***-oriented cation pairs with preset occurrence probabilities, w_{ik} and w_{ki}. The second "improvement" stage refines these cation distributions using two penalty functions (Dainyak et al. 2004). The first referred to as "diagonal limitation" regulates the occurrence of any $\boldsymbol{b_1}$- and $\boldsymbol{b_2}$-oriented (Fig. 1) cation pairs. The second one manipulates the preset number of groups of local cation arrangements according to the number of Fe^{3+} and Fe^{2+} doublets with resolved Δ_j^{fit} values in the fitted Mössbauer spectrum. Each of these groups, j, represents a combination of arrangements with similar Δ_i values. The total occurrence probabilities, W_j, for the groups summed over the individual occurrence probabilities, w_i, for the arrangements belonging to group j are compared with the corresponding doublet areas S_j. The simulated cation distribution corresponds to the minimum of the objective function *F*:

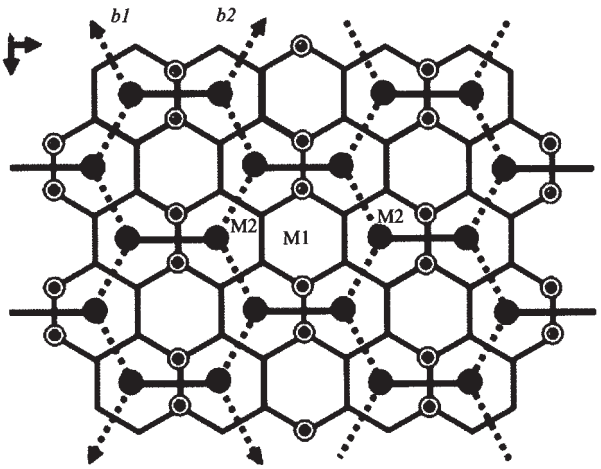

FIGURE 1. Two-dimensional distribution of cations in a *trans*-vacant octahedral sheet. Open and black circles correspond, respectively, to OH groups and octahedral cations occupying *cis*-sites.

$$F = \Sigma_j(W_j - S_j)^2 p_j,$$

where p_j is the penalty for group j.

The improvement stage is conducted using a preset number of rearrangements for the ***b***-oriented cation pairs (usually 20 000) followed by a preset number of Monte-Carlo runs (usually 100). The total number of cations involved in the simulation procedure is 1150, of which 142 are Monte-Carlo updated and 1008 are working.

To be acceptable, the simulated two-dimensional cation distributions: (1) must have a value for the function *F* not exceeding 0.05, the corresponding probability equal to 1.0, and the W_j and S_j values must be close, and (2) the statistically weighted Δ_j^{calc}

values must be close to the Δ_j^{fit} values for Fe^{3+} and Fe^{2+} from computer fits of the spectra. The Δ_j^{calc} values are calculated as sums of the products of normalized occurrence probabilities w_i^n and the corresponding Δ_i values: $\Delta_j^{calc} = \Sigma\, w_i^n\, \Delta_i$. Depending on the cation type, Fe^{3+} or Fe^{2+}, either Δ_i^{pred} or Δ_i^{tent} are used, respectively.

Comparison between different approaches to evaluating Mössbauer spectra of phyllosilicates.

Two widely used methods to evaluate Mössbauer spectra are the so-called model approach and the quadrupole splitting distribution (QSD) analysis. The model approach is usually applied for elaborate crystal-chemical models when there is extensive a priori information about the objects under study. The most convenient fitting algorithm for the model approach is based on least-squares minimization methods, assuming Lorentzian or pseudo-Voigt line shapes. There are several available fitting programs. Examples of advanced sophisticated programs include the software MOESALS by Lottermoser et al. (1993), the SPECTR program from the software MSTOOLS by Rusakov and Chistyakova (1992), and the software package VI-NDA (Gunnlaugsson 1999).

The fitting of QSDs or hyperfine field distributions (HFDs) is mostly intended for analyzing spectra of locally inhomogeneous systems (phases of variable compositions, amorphous substances, such as glasses or gels, multicomponent alloys, admixture and defect systems, etc). A discrete QSD with Lorentzian line shapes was described, for example, by Wivel and Mørup (1981), and a Voigt-based method was presented by Rancourt and Ping (1991). The latest program that uses the original mathematical formalism and continuous QSDs and HFDs is described by Rusakov (1999).

Layer silicates characterized by extensive isomorphous substitutions can be considered, to some extent, as local inhomogeneous systems. Therefore, many authors considered the application of QSD analysis to be promising. However, for the purpose of investigating spectra of layer silicates, the use of QSD analysis is informative. For example, QSD analysis of spectra of trioctahedral micas leads to the conclusion that it is impossible to distinguish between *cis*- and *trans*-sites because of the influence of local environment around the Fe probe nucleus (Rancourt 1994; Redhammer 1998; Redhammer et al. 2000, 2002). Lougear et al. (2000) solved this problem for the chlorite series by using the model approach. They performed molecular orbital (MO) calculations on various model clusters and proved that different anion (OH^-) distributions in the first coordination sphere of M1, M2, and M3 positions have more influence on the Fe^{2+} quadrupole splitting than cationic disorder. According to this information, chlorite spectra were refined with a least-squares minimization program and with corresponding assignments.

Because our method (Dainyak et al. 2004) is crystal-chemically grounded and implies "fine structure" of the fitted doublets, with the a priori known individual quadrupole splittings for both Fe^{3+} and Fe^{2+} and their assignments, the model approach is the most appropriate here, whereas using QSD analysis is not expedient.

Regardless of the mathematical method for spectra fitting, the primary importance is that the results obtained are crystal-chemically consistent. This is illustrated by an example (Appendix 1) where the results of the interpretation of Mössbauer parameters obtained using different fitting programs (model approach and QSD analysis) for the same sample produced similar results.

Results

The OH-stretching region of IR spectra

The positions and relative integrated intensities of individual OH bands corresponding to specific cation-OH-cation vibrations are given in Tables 3 (the Baltic samples) and 4 (the North Sea samples). The decomposed OH-stretching regions of two Baltic samples, sample ES having 75% I and 25% S layers, and sample SL having 84% I, 12% T, and 4% S layers, are shown in Figure 2. The decomposed OH-stretching regions of two North Sea samples, sample X3 having 67% I, 8% T, and 25% (S+V) layers, and sample X18 having 71% I, 19% T, and 10% (S+V) layers, are shown in Figure 3.

For the Baltic samples, the OH-stretching region of the spectrum of the low-diagenetic sample ES, which has relatively low Al and relatively high Mg and Fe, contains a weak Fe^{2+}-OH-Fe^{3+} band at 3522 cm^{-1}, an Mg-OH-Fe^{3+} band that overlaps with Al-OH-Fe^{2+} at 3552 cm^{-1}, an Al-OH-Fe^{3+} band at 3578 cm^{-1}, an Al-OH-Mg band at 3604, and three Al-OH-Al bands at 3627, 3651, and 3677 cm^{-1} (Table 3). The third Al-OH-Al band may refer to pyrophyllite-like structural fragments within the dehydrated I-T-S structure (Besson and Drits 1997a, 1997b; Zviagina et al. 2004). The OH-stretching regions of the spectra of samples AA, OL, SL, and OS, which are close in chemical composition (Table 1), are similar. They contain three Al-OH-Al bands at about 3628, 3648, and 3663 cm^{-1}, an Al-OH-Mg band at 3604–3609 cm^{-1}, an Al-OH-Fe^{3+} band at 3577–3580 cm^{-1}, and an Al-OH-Fe^{2+} band at 3552–3555 cm^{-1}. In addition, these spectra contain a band at about 3690–3697 cm^{-1}. This band also may be associated with the possible presence of pyrophyllite-like structural domains, although its origin remains somewhat problematic (Zviagina et al. 2004). Minor bands observed in the high-wavenumber region (>3700 cm^{-1}) in some of the spectra may be artifacts resulting from the use of a strictly Gaussian peak shape. Their contributions are, however, negligible and have not been included in the spectra decomposition.

All North Sea samples except X18 contain kaolinite, which is observed as sharp peaks at about 3700 cm^{-1} and, in the case of sample 82, also at about 3622 cm^{-1}. The contribution of kaolinite Al-OH-Al vibrations was subtracted from the total integrated

Table 3. Infrared spectroscopy of the Cambrian samples

	Sample									
	AA		OL		SL		OS		ES	
Band	cm^{-1}	%	cm^{-1}	%	cm^{-1}	%	cm^{-1}	%	cm^{-1}	%
$Fe^{2+}OHFe^{3+}$	–	–	–	–	–	–	–	–	3522	1.8
$AlOHFe^{2+}$	3554	1.6	3552	1.6	3561	2.9	3552	1.8	3552	2.8
$MgOHFe^{3+}$	–	–	–	–	–	–	–	–	3552	3.0
$AlOHFe^{3+}$	3580	4.3	3580	4.5	3580	3.0	3577	4.9	3578	11.8
AlOHMg	3607	21.1	3609	25.0	3604	19.1	3604	25.8	3604	26.2
AlOHAl	3628	32.0	3628	26.6	3626	35.3	3626	39.1	3627	27.2
AlOHAl	3646	12.6	3646	12.8	3652	21.1	3649	18.2	3651	18.6
AlOHAl	3662	24.4	3662	23.0	3666	12.9	3664	7.8	3677	8.5
AlOHAl	3697	3.9	3697	6.6	3696	4.8	3690	2.2	–	–

Note: Positions and relative integrated intensities (%) of OH-stretching bands corresponding to specific OH-bonded cation pairs in the spectra.

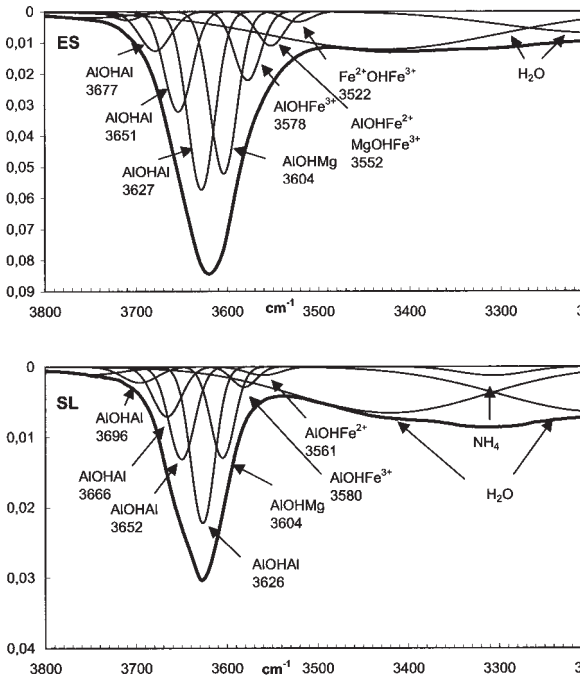

FIGURE 2. Decomposition of the IR spectra of samples ES (**a**) and SL (**b**).

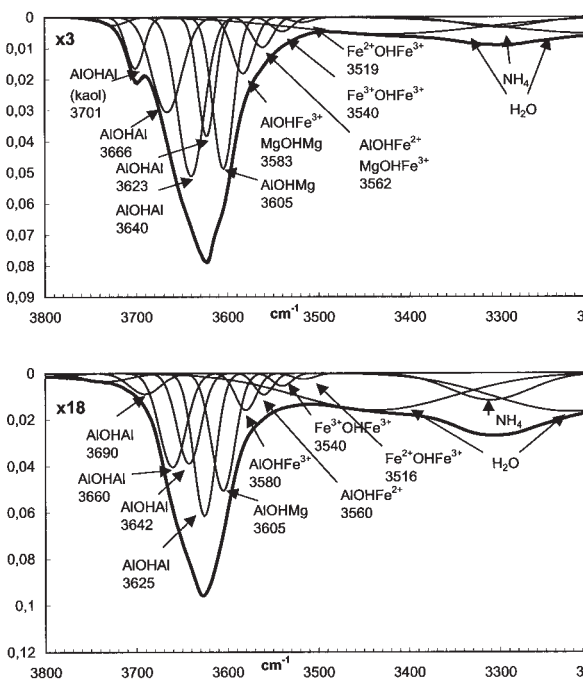

FIGURE 3. Decomposition of the IR spectra of samples X3 (**a**) and X18 (**b**).

intensity of the Al-OH-Al bands to obtain the best possible agreement between the cation compositions of the I-S samples obtained from the IR data and from the crystal-chemical formulae (Table 1). For kaolinite-bearing samples, the total relative integrated intensities of three Al-OH-Al bands (at about 3623, 3645, and 3665–3670 cm^{-1}) corresponding to the I-T-S component are shown in Table 4. Kaolinite-free sample X18 shows an additional Al-OH-Al band at 3690 cm^{-1}, which may refer to pyrophyllite-like domains within the I-T-S-structure (Zviagina et al. 2004). In accordance with relatively high Fe contents in the North Sea samples, all the spectra, in addition to the Al-OH-Al bands and an Al-OH-Mg band at 3601–3605 cm^{-1}, contain an Al-OH-Fe^{3+} band at about 3580 cm^{-1}, an Fe^{3+}-OH-Fe^{3+} band at 3540 cm^{-1}, and an Fe^{2+}-OH-Fe^{3+} band at 3516–3519 cm^{-1}. The peak at 3558–3662 cm^{-1} was assigned to the Al-OH-Fe^{2+} vibration for samples 89 and X18, to the Mg-OH-Fe^{3+} vibration in sample 112, and to a superposition of the Al-OH-Fe^{2+} and Mg-OH-Fe^{3+} bands in the rest of the North Sea samples (Table 4). The relatively high Mg contents in samples X3 and 82 can be accounted for only if the band at 3583 cm^{-1} is interpreted as a superposition of Al-OH-Fe^{3+} and Mg-OH-Mg bands.

The octahedral cation compositions of the samples calculated from the relative integrated intensities of the bands corresponding to various types of OH-bonded cation pairs are in good agreement with the crystal-chemical formulae (Table 5). In both series, all the spectra except that of ES show a broad pronounced band at about 3305–3313 cm^{-1}, which refers to the stretching vibration of fixed ammonium (Figs. 2b, 3a, and 3b).

Fitting of the Mössbauer spectra and cation distribution simulation

The Mössbauer spectra of the samples have similar observed parameters for Fe^{3+} and Fe^{2+} components, the spectra for Jurassic and Cambrian series being shown in Figures 4 and 5, respectively. The main differences in the spectra are the relative intensities of Fe^{2+} components and the position of a "saddle" of superimposed Fe^{3+} doublets at the intensity scale. The smaller the Fe content in octahedra, the larger the relative areas of the Fe^{2+} components, and the lower the position of the "saddle" (Table 1, Figs. 4 and 5).

The fitting model including two or three doublets for Fe^{3+} and one or two doublets for Fe^{2+} proved to be optimal. To fit the spectra, intermediate runs of the cation distribution simulation program were taken into account. For example, a very low Fe^{3+} content in sample SL and lack of the Fe^{3+}-OH-Fe^{3+} bands in its IR spectrum make the local cationic arrangement $3Fe^{3+}$ around Fe^{3+} impossible and the arrangement $2Fe^{3+}Al$ around Fe^{3+} improbable. As the corresponding individual doublets have the Δ_i^{pred} values 0.17 and 0.33 mm/s (Table 2), the doublet with the expected Δ_j value of about 0.30 mm/s was not included in the fitting procedure.

Mössbauer parameters for the Jurassic and the Cambrian series are shown in Table 6. Each Fe^{3+} doublet, independent of the series, is defined by a specific range of Δ_j values: 0.25–0.32, 0.46–0.69, and 1.05–1.24 mm/s (denoted by A, B, and C, respectively). Specific ranges of Δ_j values for Fe^{2+} are 2.68–2.87 and 2.13–2.50 mm/s (denoted by D and E, respectively). Thus, the

TABLE 4. Infrared spectroscopy of the Jurassic samples

	Sample											
	89		X18		X6		87		X3		82	
Band	cm^{-1}	%	cm^{-1}	%	cm^{-1}	%	cm^{-1}	%	cm^{-1}	%	cm^{-1}	%
$Fe^{2+}OHFe^{3+}$	3517	1.1	3516	1.1	3517	2.1	3519	2.0	3519	1.0	3519	2.1
$Fe^{3+}OHFe^{3+}$	3540	1.8	3540	2.0	3540	3.2	3540	3.2	3540	2.6	3540	4.6
$AlOHFe^{2+}$	3558	2.0	3560	3.2	3562	3.0	3560	2.3	3562	1.0	3561	4.0
$MgOHFe^{3+}$	–	–	–	–	3562	2.7	3560	2.3	3562	4.4	3561	4.8
$AlOHFe^{3+}$	3580	6.0	3580	6.1	3580	5.9	3580	9.5	3583	7.3	3583	8.7
MgOHMg	–	–	–	–		–	–	–	3583	3.0	3583	5.2
AlOHMg	3602	13.0	3605	21.9	3604	25.7	3602	19.9	3605	27.0	3601	19.0
AlOHAl	3625	} 76.1	3625	24.4	3625	} 57.4	3624	} 60.8	3623	} 53.7	3622	} 51.6
AlOHAl	3644		3642	16.8	3643		3646		3640		3649	
AlOHAl	3663		3660	19.5	3663		3669		3666		3675	
AlOHAl			3690	5.0								
$A(AlOHAl)_{total}$*	1.604				6.618		2.068		4.383		1.577	
$T_{kaolinite}$†	.22				.26		.41		.38		.55	

Notes: Positions and relative integrated intensities (%) of OH-stretching bands corresponding to specific OH-bonded cation pairs in the spectra. The total integrated intensities of Al-OH-Al stretching vibrations in kaolinite-bearing samples and the proportions of kaolinite contribution substracted from this intensity are given in the last two rows.

* Total integrated intensity of AlOHAl stretching vibrations in kaolinite-bearing samples (absorbance units).

† Proportion of kaolinite contribution subtracted from $A(AlOHAl)_{total}$, with subsequent normalization of 100%.

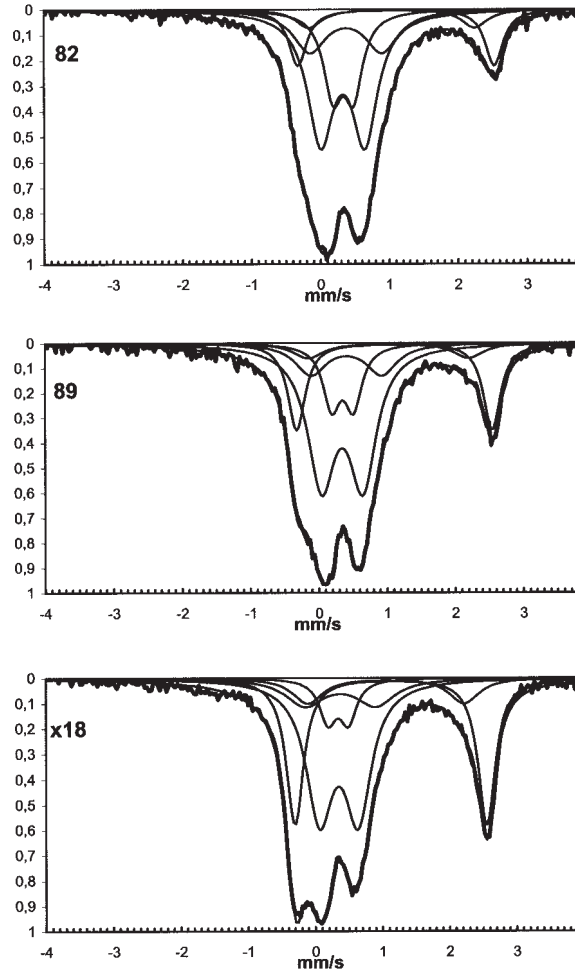

FIGURE 4. Lorentzian-based fits to the RT Mössbauer spectra of samples 82, 89, and X18 (Upper Jurassic series).

model for fitting the Mössbauer spectra proved to be nearly the same for all the studied samples. For the Fe^{3+} peaks, normalized S_A^n values gradually decrease from 0.33 to 0.00; S_B^n decreases and S_C^n is nearly constant for the Jurassic series, whereas S_B^n decreases and S_C^n increases for the Cambrian series.

TABLE 5. Octahedral cation compositions [atoms per $O_{10}(OH)_2$] obtained from chemical analysis and calculated from relative integrated intensities of OH-stretching bands

	Al		Fe^{3+}		Fe^{2+}		Mg	
Sample	chem	IR	chem	IR	chem	IR	chem	IR
Jurassic series								
X3	1.42	1.43	0.19	0.18	0.03	0.02	0.37	0.37
82	1.35	1.35	0.25	0.25	0.06	0.06	0.34	0.34
X6	1.46	1.49	0.17	0.17	0.06	0.05	0.31	0.29
87	1.51	1.53	0.22	0.21	0.07	0.04	0.20	0.22
89	1.69	1.73	0.12	0.11	0.04	0.03	0.14	0.13
X18	1.63	1.63	0.09	0.11	0.06	0.04	0.22	0.22
112	1.54	1.50	0.20	0.24	0.02	0.02	0.24	0.24
Cambrian series								
ES	1.49	1.49	0.18	0.17	0.06	0.05	0.27	0.29
OL	1.71	1.69	0.05	0.04	0.02	0.02	0.22	0.25
AA	1.72	1.73	0.05	0.04	0.02	0.02	0.21	0.21
OS	1.69	1.67	0.03	0.05	0.03	0.02	0.25	0.26
SL	1.73	1.74	0.04	0.04	0.04	0.03	0.19	0.19

The cation distribution simulation using the IR data (Tables 3 and 4) was performed simultaneously with respect to Fe^{3+} and Fe^{2+}. Two extreme cases were considered: (1) R^{2+} and R^{3+} cations having equal probability for occupancy of sites M2 and M2', and (2) R^{2+} cations having a preference for one of the sites. The individual Δ_i^{pred} for Fe^{3+} are grouped into two or three groups and the Δ_i^{tent} for Fe^{2+} into one or two groups (Table 2). Each group combines Δ_i values corresponding to one of the three ranges for fitted Δ_j Fe^{3+} values or to one of the two ranges for fitted Δ_j Fe^{2+} values. The content of these preset groups was adjusted to make the cation distribution model fit the Mössbauer parameters. Controlling of the cation distribution simulation both with Fe^{2+} and Fe^{3+} cations required a few run cycles of the program to satisfy spectral parameters.

The results of the cation distribution simulation are shown in Table 7. For the Fe^{3+} groups A, B, and C, the total occurrence probabilities W_A, W_B, and W_C summed over the simulated occurrence probabilities, w_i, are equal or approximately equal to the corresponding doublet areas S_A, S_B, and S_C. For the Fe^{2+} groups D and E, the occurrence probabilities W_D and W_E are also equal to the corresponding doublet areas S_D and S_E except for samples 87, 89, and SL. This discrepancy is, like the broadened region of Δ_j for the E doublet, due to the small amount of Fe^{2+}. The statistically weighted quadrupole splittings Δ_j^{calc} (j = A, B, C, D, and

TABLE 6. Mössbauer parameters for the Jurassic and Cambrian samples arranged according to increasing degree of diagenetic transformation and decreasing Fe content in octahedra, respectively

Sample	ΣFe	Fe^{3+}					Fe^{2+}						
		Doublet	δ*	Δ†	Γ‡	S^n†	Doublet	δ*	Δ†	Γ‡	S^n§	Fe^{3+}/Fe^{2+}	χ^2
Jurassic series													
X3	0.18	A	0.36	0.30	0.33	0.33	D	1.14	2.78	0.37	0.71		
		B	0.36	0.67	0.43	0.52	E	0.98	2.32	0.42	0.29	3.31	1.28
		C	0.36	1.24	0.57	0.15							
82	0.31	A	0.36	0.30	0.33	0.24	D	1.13	2.85	0.31	0.68		
		B	0.36	0.64	0.46	0.54	E	1.07	2.41	0.46	0.32	4.1	1.10
		C	0.40	1.05	0.58	0.22							
X6	0.23	A	0.37	0.30	0.28	0.24	D	1.14	2.87	0.30	0.70		
		B	0.36	0.69	0.50	0.58	E	1.08	2.51	0.41	0.30	3.06	1.30
		C	0.48	1.05	0.67	0.17							
87	0.25	A	0.36	0.31	0.33	0.21	D	1.13	2.85	0.33	0.76		
		B	0.36	0.64	0.47	0.53	E	1.06	2.30	0.50	0.24	2.97	1.34
		C	0.41	1.07	0.55	0.26							
89	0.16	A	0.37	0.32	0.30	0.18	D	1.13	2.86	0.30	0.76		
		B	0.36	0.62	0.49	0.65	E	1.04	2.36	0.54	0.24	2.9	1.02
		C	0.44	1.04	0.54	0.17							
X18	0.15	A	0.37	0.30	0.32	0.13	D	1.16	2.85	0.32	0.77		
		B	0.38	0.58	0.48	0.67	E	1.08	2.32	0.54	0.23	1.58	2.1
		C	0.40	1.06	0.70	0.20							
Cambrian series													
ES	0.22	A	0.38	0.25	0.32	0.04	D	1.15	2.69	0.42	0.82		
		B	0.38	0.56	0.49	0.67	E	1.07	2.13	0.57	0.18	2.96	0.87
		C	0.40	1.18	0.61	0.29							
KV	0.20	A	0.37	0.30	0.30	0.09	D	1.14	2.68	0.40	0.82	3.1	1.72
		B	0.37	0.60	0.50	0.51	E	1.04	2.17	0.50	0.18		
		C	0.40	1.14	0.66	0.40							
KI	0.18	B	0.38	0.54	0.51	0.69	D	1.16	2.79	0.38	0.64	3.5	1.16
		C	0.42	1.14	0.68	0.11	E	1.02	2.42	0.48	0.36		
OL	0.07	A	0.31	0.31	0.29	0.03	D	1.16	2.81	0.34	0.72		
		B	0.36	0.58	0.58	0.57	E	1.01	2.31	0.51	0.28	2.7	1.09
		C	0.38	1.17	0.62	0.40							
AA	0.07	B	0.37	0.54	0.59	0.68	D	1.16	2.82	0.40	0.84	3.02	1.07
		C	0.38	1.21	0.68	0.32	E	1.02	2.30	0.40	0.16		
OS	0.07	B	0.37	0.54	0.54	0.64	D	1.16	2.85	0.54	1.	4.32	2.86
		C	0.38	1.17	0.66	0.36							
SL	0.07	B	0.37	0.46	0.48	0.44	D	1.16	2.87	0.29	0.85	1.12	1.05
		C	0.40	1.07	0.62	0.56	E	1.07	2.50	0.42	0.15		

* Isomer shift vs. αFe, mm/s.
† Quadrupole splitting.
‡ Full width at half-maximum, mm/s.
§ Normalized areas under doublet peaks.

E) are close to the corresponding Δ_j values from the computer fits to the spectra. A detailed example of Δ_j^{calc} calculations for one of the most Fe-rich samples, X3, is given in Table 2. The table contains Δ_i^{pred} and Δ_i^{tent} values used to calculate Δ_j^{calc} values for Fe^{3+} and Fe^{2+}, respectively. It also includes the simulated individual occurrence probabilities, w_i, with their grouping, the normalized w_i^n values and the intermediate steps for the Δ_j^{calc} calculations. The resulting Δ_j^{calc} values for the doublets A, B, C, D, and E fitted to the Mössbauer spectrum are shown at the bottom of Table 2.

DISCUSSION

Interpretation of IR spectra

For all monomineral, kaolinite-free samples (the Baltic series and sample X18 of the North Sea series), good agreement between the octahedral cation compositions calculated from the IR data and those given by crystal-chemical formulae was obtained for samples of diverse compositions using one set of individual OH band positions that vary within narrow wavenumber intervals (Table 8). The fit of octahedral cation compositions can therefore be regarded as a reliable criterion for the validity of the resulting OH band identification, and the ambiguity in spectra

TABLE 7. Comparison of the total simulated occurrence probabilities, W_j, for the groups and statistically weighted quadrupole splittings, Δ_j^{calc}, with the relative doublet areas, S_j^{fit}, and quadrupole splittings, Δ_j^{fit}, from computer fits to the spectra, respectively, for Fe^{3+} and Fe^{2+}

Sample	Fe^{3+}					Fe^{2+}				
	j	W_j	S_j^{fit}	Δ_j^{calc}	Δ_j^{fit}	j	W_j	S_j^{fit}	Δ_j^{calc}	Δ_j^{fit}
X3	A	0.313	0.33	0.31	0.30	D	0.700	0.71	2.84	2.78
	B	0.538	0.52	0.65	0.67	E	0.300	0.29	2.27	2.32
	C	0.150	0.15	1.18	1.24					
82	A	0.241	0.24	0.31	0.30	D	0.677	0.68	2.84	2.85
	B	0.542	0.54	0.65	0.64	E	0.299	0.32	2.31	2.41
	C	0.217	0.22	1.03	1.05					
X6	A	0.242	0.24	0.30	0.30	D	0.686	0.70	2.87	2.87
	B	0.579	0.58	0.66	0.69	E	0.314	0.30	2.31	2.51
	C	0.174	0.17	1.04	1.05					
87	A	0.203	0.21	0.31	0.31	D	0.630	0.76	2.83	2.85
	B	0.525	0.53	0.62	0.64	E	0.37	0.24	2.30	2.30
	C	0.257	0.26	1.22	1.07					
89	A	0.176	0.18	0.33	0.32	D	0.667	0.76	2.84	2.86
	B	0.642	0.65	0.59	0.62	E	0.334	0.24	2.34	2.36
	C	0.180	0.17	1.06	1.04					
X18	A	0.129	0.13	0.31	0.30	D	0.762	0.77	2.84	2.85
	B	0.671	0.67	0.54	0.58	E	0.238	0.23	2.25	2.32
	C	0.196	0.20	1.03	1.06					
ES	A	0.024	0.04	0.30	0.25	D	0.829	0.82	2.67	2.69
	B	0.687	0.67	0.53	0.56	E	0.171	0.18	1.85	2.13
	C	0.287	0.29	1.19	1.18					
SL	B	0.441	0.44	0.45	0.46	D	0.806	0.85	2.84	2.87
	C	0.559	0.56	1.08	1.07	E	0.194	0.15	2.49	2.50

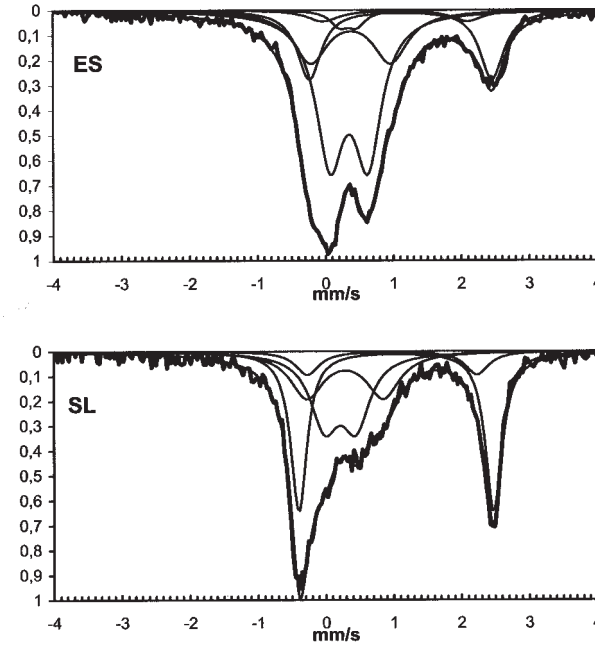

FIGURE 5. Lorentzian-based fits to the RT Mössbauer spectra of samples ES and SL (Cambrian series).

decomposition imposed by the poor resolution of I-S spectra was thus minimized. Accordingly, the spectra of kaolinite-bearing samples from the North Sea series were treated with one set of band assignments and the contribution of kaolinite Al-OH-Al vibrations was subtracted from the total integrated intensity of the Al-OH-Al bands. This approach also made it possible to interpret the low intensity bands in the low-wavenumber region present in most spectra (Tables 3 and 4, Figs. 2 and 3).

The positions of individual bands agree well with those found for dioctahedral micas (Table 8). The Fe^{3+}-OH-Fe^{3+} and Al-OH-Fe^{3+} bands, however, are shifted toward greater wavenumbers (3540 and 3580 vs. 3535 and 3573 cm^{-1} in micas, respectively). These shifts may be due to the presence of smectite interlayers, as the OH-stretching bands involving Fe in dioctahedral smectites were shifted to greater wavenumbers relative to the corresponding mica OH (Zviagina et al. 2002, 2004). The shift of the Al-OH-Fe^{3+} band to about 3580 cm^{-1} results in possible overlap with the Mg-OH-Mg band (3583 cm^{-1}).

In the case of samples X3 and 82, the high contents of Mg [0.34 and 0.37 atoms per $O_{10}(OH)_2$, respectively] can be explained only if the band at 3583 cm^{-1} is interpreted as superposition of Al-OH-Fe^{3+} and Mg-OH-Mg stretching vibrations. The possible presence of OH-linked MgMg cation pairs in the octahedral sheets of dioctahedral 2:1 phyllosilicates has been discussed extensively in the literature. Using quantum mechanical calculations of structural models of dioctahedral phyllosilicates in the illite-smectite series, Sainz-Diaz et al. (2002, 2003a, 2003b) and Timon et al. (2003) showed that Mg cations tend to be dispersed in the octahedral sheet in contrast to Fe cations that have a tendency to clustering. In contrast, Besson and Drits (1997a) found Mg-OH-Mg stretching bands

TABLE 8. Mean positions of OH-stretching bands corresponding to specific cation pairs for dioctahedral micas and I-T-S

Band	Mica*	e.s.d.‡	I-T-S†	e.s.d.‡
$Fe^{2+}OHFe^{3+}$	3521	3	3518	2
$Fe^{3+}OHFe^{3+}$	3535	2	3540	0
$MgOHFe^{3+}$				
$AlOHFe^{2+}$	3559	3	3558	4
$AlOHFe^{3+}$	3573	2	3580	2
MgOHMg	3583	3	3583	0
AlOHMg	3604	3	3604	2
AlOHAl	3621	4	3625	2
AlOHAl	3641	3	3646	4
AlOHAl	3658	3	3664	3
pyr.-like				
AlOHAl	3675	4	3676	1
AlOHAl			3694	4

* Besson and Drits (1997a).
† This work.
‡ Estimated standard deviations for OH band positions in I-T-S spectra (cm^{-1}).

in the IR spectra of Mg-rich dioctahedral micas. Similarly, in a recent study of clay minerals at the Cretaceous/Tertiary boundary in Denmark (Drits et al. 2004), the strong band at 3585 cm^{-1} in the IR spectrum of montmorillonite HSI was attributed to the Mg-OH-Mg stretching vibration. The Mg-OH-Mg band was also identified in the spectra of four Mg-rich montmorillonites (Montmorillon, Polkville, SAz-1, and Otay) studied by Zviagina et al. (2002, 2004). Indirect but strong theoretical and experimental evidence for the existence of Mg-OH-Mg pairs in dioctahedral smectites was obtained by Méring and Glaeser (1954). These authors showed that different proportions of interlayer Ca cations are required to provide local compensation of the 2:1 layer negative charge originating from Mg-OH-Mg pairs in *trans*-vacant (*tv*) and *cis*-vacant (*cv*) montmorillonites containing the same amount of randomly distributed octahedral Mg (Fe^{2+}) and Al (Fe^{3+}) cations. They showed experimentally that for *cv* montmorillonite from Camp-Bertaux, the proportion of interlayer Ca cations necessary for local compensation of the Mg-OH-Mg negative charge exactly corresponded to the amount of Mg-OH-Mg cationic pairs that should be observed for random distribution of octahedral di- and trivalent cations. Taking this into account, the assignment of the band at 3583 cm^{-1} in samples X3 and 82 to superposition of Al-OH-Fe^{3+} and Mg-OH-Mg stretching vibrations appears justified.

R^{2+} preference for either *cis*-site

Preference or indifference of R^{2+} to one of two *cis*-positions are options used by the cation distribution simulation program as a base for all further manipulations. Previously, for Fe-rich glauconites, celadonites, and Fe^{3+}-rich illites, the preference of R^{2+} to one of the *cis*-positions was unambiguous (Drits et al. 1997a; Dainyak et al. 2004). Because of the low Fe content in the studied samples and because the local two-dimensional cation arrangements around Mg or Al cations cannot be controlled in our simulation program, the choice between these options was problematic. Simulation of the cation distributions with and without preference of R^{2+} for one of the two symmetrically independent *cis*-sites has shown that a good agreement between W_j and S_j^{fit} values and between Δ_j^{calc} and Δ_j^{fit} values can be obtained for both models. However, omitting preset R^{2+} preference to one of the *cis*-sites leads to a significant increase in the objective function controlling the cation distribution simulation process,

and to significantly increasing the occurrence probabilities, w_i, for the local arrangements 3Mg, 2MgAl, and 2AlMg around Mg responsible for Mg-clustering. Thus, the preset indifference of R^{2+} to one of the *cis*-positions yields cation distributions with large Mg clusters. These Mg-clusters, however, are unlikely because of the tendency for homogeneous dispersion of octahedral charge, as observed for glauconite, celadonite, Fe^{3+}-rich illite, and leucophyllite (Drits et al. 1997a; Dainyak et al. 2004). Suppressing the $\boldsymbol{b_1}$-, $\boldsymbol{b_2}$-oriented MgMg pairs leads, however, to W_j values that differ considerably from corresponding S_j^{fit}.

Based on the principle of homogeneous dispersion of octahedral charge and on the two criteria for accepting the cation distributions, R^{2+} preference to one of the symmetrically independent *cis*-sites is most probable.

Analysis of the two-dimensional cation distribution reconstructions

Cation distribution patterns for the end-members of the Jurassic and Cambrian series satisfying both IR and fitted Mössbauer parameters for both Fe^{3+} and Fe^{2+} are shown for the detrital samples X3 (Jurassic) and ES (Cambrian) in Figures 6a and 6c, respectively, and for the diagenetically transformed samples X18 (Jurassic) and SL (Cambrian) in Figures 6b and 6d, respectively.

For all the cation distributions, the function *F* is minimized when R^{2+} cations preferentially occupy one of the two symmetrically independent *cis*-sites in the $\boldsymbol{b}$-direction. There is thus a tendency to obey the homogeneous dispersion of octahedral charge. The Al-bearing matrix contains two main types of clusters (Fig. 6): (1) Fe clusters, and (2) much larger clusters of mixed cation composition (Mg, Al, Fe^{3+}, and Fe^{2+}) that have a tendency to regular alternation of di- and trivalent cations (hereafter referred to as ordered clusters).

Ordered clusters. The cation distributions for the Jurassic series, from X3 (67% I and 8% T layers) to X18 (71% I and 19% T layers), and the Cambrian series, from ES (75% I layers) to SL (84% I and 12% T layers), show that the diagenetic transformation involving an increase in ^{VI}Al and a decrease in Mg and Fe is accompanied by a decrease of the ordered areas (Fig. 6). For example, for the transformed sample SL having a very low Fe content [0.08 per $O_{10}(OH)_2$], the ordered clusters are present but they are fewer in number and of smaller size compared to the detrital ES having 0.24 Fe per $O_{10}(OH)_2$.

The $\boldsymbol{b}$-oriented cation pairs of the type $R^{2+}R^{3+}$ involved in ordered clustering are termed "cluster forming pairs" (cf-pairs), with the corresponding occurrence probabilities, w_{cf} A couple of the cf-pairs, which are nearest neighbors independent of the direction ($\mathbf{b}$, $\mathbf{b_1}$, or $\mathbf{b_2}$), is referred to as a minimum ordered cluster. Then the "cluster" factor, ζ, will be equal to the total number of the cf-pairs involved in ordered clusters, W_{cf}, divided by the total amount of $R^{2+}R^{3+}$ pairs, W_{IR}, determined by IR. In fact, ζ is the percentage of the $R^{2+}R^{3+}$ IR pairs involved in the ordered clustering. The ζ values and the corresponding occurrence probabilities w_{cf}, w_{IR}, W_{cf}, and W_{IR} are shown in Tables 9a and 9b. With the exception of sample 89, the ζ values are very high and independent on the Fe, Al, or Mg content in the octahedra and the degree of diagenetic transformation.

Table 9 also contains percentages of the individual cf-pairs, w_{cf}, and pairs determined by IR, w_{IR}. The ξ values are also very high for all individual cationic pairs except $Fe^{2+}Fe^{3+}$ pairs in samples 87 and 89. The $Fe^{2+}Fe^{3+}$ cf-pairs are absent in the cation distribution for the transformed Cambrian sample SL having 0.08 Fe per $O_{10}(OH)_2$. Whereas the percentage of the $MgFe^{3+}$ pairs decreases for this sample, and the $MgFe^{3+}$ pairs are absent in the transformed samples 89 and X18 of the Jurassic series having 0.16 and 0.15 Fe per per $O_{10}(OH)_2$, respectively. Thus, during diagenesis, ordered clusters "melt" and "crumble" but still exist with high values of the cluster factor.

Fe^{3+} clusters. For the detrital Jurassic sample X3 [1.42 ^{VI}Al, 0.19 Fe^{3+}, 0.03 Fe^{2+} per $O_{10}(OH)_2$], small Fe^{3+} clusters form associations of Fe-Fe pairs oriented in the $\boldsymbol{b_1}$, $\boldsymbol{b_2}$, and $\boldsymbol{b}$ directions (Fig. 6a). For the detrital Cambrian samples ES, [1.49 ^{VI}Al, 0.18 Fe^{3+}, 0.06 Fe^{2+} per $O_{10}(OH)_2$] in accordance with the IR data, $Fe^{3+}OHFe^{3+}$ configurations are absent and the cation distributions contain short chains consisting of two Fe-Fe pairs oriented alternatively along the $\boldsymbol{b_1}$ and $\boldsymbol{b_2}$ directions. Most of Fe^{3+} cations in the distribution form isolated Fe-Fe pairs oriented either in the $\boldsymbol{b_1}$ or in $\boldsymbol{b_2}$ directions (Fig. 6c).

Diagenesis of the Jurassic samples by transformation of 12% (S+V) layers to T layers is accompanied by destruction of the Fe^{3+} clusters. The cation distribution of the transformed sample X18 [1.63 ^{VI}Al, 0.09 Fe^{3+}, 0.03 Fe^{2+} per $O_{10}(OH)_2$] (Fig. 6b) contains either short chains consisting of two Fe-Fe pairs or isolated Fe-Fe pairs oriented along the $\boldsymbol{b}$, $\boldsymbol{b_1}$, and $\boldsymbol{b_2}$ directions. Thus, during the diagenetic transformation of Cambrian samples involving the transformation of 15% S layers to T layers, an increase in ^{VI}Al from 1.49 to 1.73 and a decrease in Mg of 0.08, per $O_{10}(OH)_2$, only the relative amounts of the chains and isolated Fe-Fe pairs decrease (Fig. 6d). The diagenetic transformation in these I-S from shales is therefore different from the transformation of I-S in bentonites, which, according to Cuadros et al. (1999), Sainz-Diaz et al. (2003a, 2003b), and Timon et al. (2003), involves an increased tendency to Fe segregation in octahedra.

Mechanism of octahedral cation redistribution. The transformation of S to T layers in the Jurassic and Cambrian samples is accompanied by decreasing w_{cf} values for $MgFe^{3+}$ and $Fe^{2+}Fe^{3+}$ pairs (Table 9). This change reflects a decreasing size of the ordered clusters due to replacement of Fe and Mg by Al in the octahedral sheets (Table 9). At the same time, the normalized occurrence probabilities for cf-pairs, w_{cf}^n, are approximately the same for all studied samples (Table 10). Only highly transformed samples lack the cf-pairs $MgFe^{3+}$ and $Fe^{2+}Fe^{3+}$, which have low-occurrence probabilities even for the low-diagenetic samples. Thus, despite decreasing size of the ordered clusters during diagenesis their composition is largely constant. Accordingly, the main octahedral cation redistribution occurs not within the clusters but at their edges, such that Mg and Fe cations located at these edges are replaced by Al. It is remarkable that the constant composition of the ordered clusters is common both for Jurassic and Cambrian samples, and thus the main mechanism of the cation redistribution occurring for all studied samples is replacement of Mg and Fe by Al at the cluster edges.

With increasing degree of diagenesis of the Jurassic series, from 65% I and 8% T layers to 65% I and 20% T layers, degeneration of Fe^{3+}-clusters is reflected by a decrease in the occurrence probability, w_i, for the arrangement $2Fe^{3+}Al$ around Fe^{3+}. Parallel

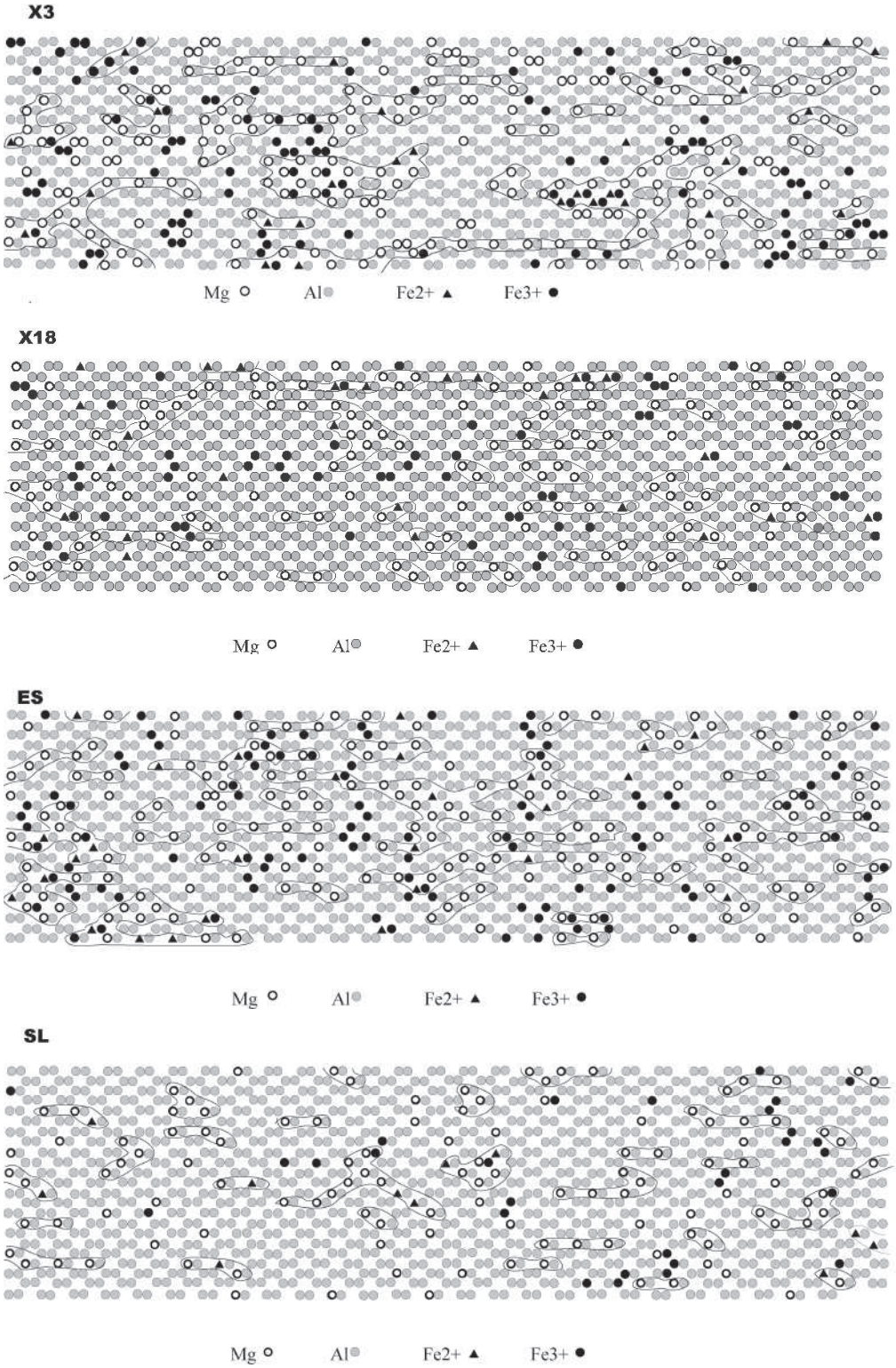

FIGURE 6. Patterns of two-dimensional cation distribution derived for samples X3 (**a**), X18 (**b**), ES (**c**) and SL (**d**).

TABLE 9A. Jurassic samples

Cation	X3			82			X6			87			89			X18		
Pair	w_{cf}	w_{IR}	%*	w_{cf}	w_{IR}	%*	w_{cf}	w_{IR}	%*	w_{cf}	w_{IR}	%*	w_{cf}	w_{IR}	%*	w_{cf}	w_{IR}	%*
MgAl	0.225	0.269	84	0.159	0.189	84	0.250	0.257	97	0.164	0.198	83	0.076	0.130	58	0.182	0.220	83
Fe^{2+}Al	0.029	0.030	97	0.034	0.041	83	0.027	0.030	90	0.022	0.023	96	0.013	0.020	65	0.024	0.032	75
$MgFe^{3+}$	0.019	0.024	79	0.034	0.048	71	0.027	0.027	100	0.019	0.023	83	–	–	–	–	–	–
$Fe^{2+}Fe^{3+}$	0.008	0.010	80	0.018	0.021	86	0.016	0.021	76	0.008	0.020	40	0.002	0.011	18	0.010	0.011	91
	W_{cf}	W_{IR}		W_{cf}	W_{IR}		W_{cf}	W_{IR}		W_{cf}	W_{IR}		W_{cf}	W_{IR}		W_{cf}	W_{IR}	
$R^{2+}R^{3+}$	0.281	0.333		0.245	0.299		0.320	0.335		0.213	0.264		0.091	0.161		0.216	0.263	
ζ		84%			82%			95%			81%			57%			82%	

Notes: Occurrence probabilities for the simulated cluster forming cation pairs, w_{cf}, and for cation pairs $R^{2+}R^{3+}$ fitted to the IR spectra, w_{IR}, and corresponding total occurrence probabilities, W_{cf} and W_{IR}, and cluster factor ζ.
* Percentage of the individual cluster forming pair.

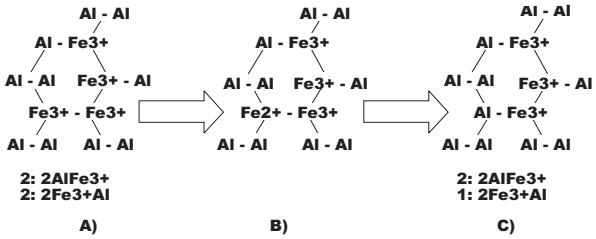

FIGURE 7. Mechanism of the Fe^{3+} reduction-replacement during diagenetic transformations of I-S.

TABLE 9B. Cambrian samples

Cation	ES			SL		
pair	w_{cf}	w_{IR}	%*	w_{cf}	w_{IR}	%*
MgAl	0.250	0.263	95	0.135	0.190	71
Fe^{2+}Al	0.029	0.028	100	0.016	0.020	80
$MgFe^{3+}$	0.029	0.030	97	0.005	0.010	50
$Fe^{2+}Fe^{3+}$	0.013	0.018	72	–	–	–
	W_{cf}	W_{IR}		W_{cf}	W_{IR}	
$R^{2+}R^{3+}$	0.321	0.339		0.156	0.220	
Z		95%			71%	

Notes: Occurrence probabilities for the simulated cluster forming cation pairs, w_{cf}, and for cation pairs $R^{2+}R^{3+}$ fitted to the IR spectra, w_{IR}, and corresponding total occurrence probabilities, W_{cf} and W_{IR}, and cluster factor ζ.
* Percentage of the individual cluster forming pairs.

TABLE 10. Normalized occurrence probabilities, w_{cf}^{n}, for cluster forming pairs

Cluster forming pair	X3	82	X6	87	89	X18	ES	SL
MgAl	0.80	0.65	0.78	0.77	0.84	0.84	0.78	0.86
Fe^{2+}Al	0.10	0.14	0.08	0.10	0.14	0.11	0.09	0.10
$MgFe^{3+}$	0.07	0.14	0.08	0.09	–	–	0.09	0.03
$Fe^{2+}Fe^{3+}$	0.03	0.07	0.05	0.04	0.02	–	0.04	–

TABLE 11. Simulated occurrence probabilities, w_i, for the most meaningful or indicative cationic arrangements around the cations Fe^{3+}, Fe^{2+}, and Mg

Arrangement	Upper Jurassic series						Cambrian series	
	X3	82	X6	87	89	X18	ES	SL
Fe^{3+} centered								
$2Fe^{3+}$Al	0.241	0.188	0.183	0.195	0.168	0.104	0.017	0.038
$2AlFe^{3+}$	0.145	0.177	0.185	0.260	0.432	0.584	0.476	0.356
3Al	0.245	0.155	0.203	0.150	0.153	0.007	0.013	0.113
Fe^{2+} centered								
$2Fe^{3+}$Al	0.075	0.106	0.100	0.110	0.067	0.076	0.161	–
$2AlFe^{3+}$	0.205	0.174	0.292	0.260	0.260	0.162	0.391	0.200
3Al	0.670	0.674	0.600	0.545	0.667	0.733	0.435	0.800
Mg centered								
$2AlFe^{3+}$	0.193	0.210	0.253	0.213	0.118	0.156	0.167	0.151
3Al	0.547	0.312	0.721	0.746	0.882	0.819	0.768	0.849
2AlMg	0.146	0.205	–	0.016	–	0.008	0.006	–

to this, w_i for $2AlFe^{3+}$ increases significantly (Table 11). Figure 7a shows a Fe^{3+}-cluster consisting of three simple Fe^{3+}-Fe^{3+} links including arrangements $2AlFe^{3+}$ and $2Fe^{3+}Al$. Based on the w_i values for these arrangements, the Fe-release process may be that, during the diagenetic transformation, first Fe^{3+} is partially reduced to Fe^{2+}. Because the $\boldsymbol{b_1}$-, $\boldsymbol{b_2}$-oriented Fe^{3+}-Fe^{3+} bonds are the most stable bonds in the high-transformed samples (Figs. 6b and 6d), the Fe^{3+} may be reduced in the $\boldsymbol{b}$-oriented Fe^{3+}-OH-Fe^{3+} groups (Fig. 7b). Then, the newly formed Fe^{2+} cation, which has the largest size in this cation distribution fragment, may be replaced by an Al cation. This reaction results in a relative increase of $2AlFe^{3+}$ and a decrease of $2Fe^{3+}Al$ arrangements (Fig. 7c), which is in agreement with Table 11. The IR data presented in Table 4 support such a mechanism: the occurrence probabilities w_{ik} for the Fe^{3+}-OH-Fe^{3+} and Fe^{2+}-OH-Fe^{3+} groups decrease for the Jurassic series with the transformation of S layers to T layers. In addition, the intensive Fe^{3+} reduction-release process is important in the arrangements 3Al, as seen from the decreasing w_i values (Table 11).

This mechanism explains the relative increase of Fe^{2+} during transformation. Table 11 shows that the occurrence probabilities for the arrangements $2Fe^{3+}Al$, $2AlFe^{3+}$, and 3Al around Fe^{2+} change only slightly implying the survival of Fe^{2+} in these three arrangements. Thus, the local arrangement consisting of three trivalent cations around Fe^{2+} is the most stable. The Fe^{2+} preservation in the ordered clusters masks the Fe^{3+} reduction-release process.

As mentioned above, Cambrian samples display a different initial Fe^{3+} clustering and, as a consequence, the behavior of the arrangements around Fe^{3+} differs from that of the Jurassic series. The w_i values for the arrangements $2AlFe^{3+}$ around Fe^{3+} and Fe^{2+} decrease significantly with increasing transformation, from 75% I layers to 80% I layers and 15% T layers (Table 11), whereas the w_i values for the arrangements 3Al around these cations increase. This cation reorganization is probably due to reduction of Fe^{3+} in the arrangement $2AlFe^{3+}$ and subsequent replacement by Al.

Behavior of the local cation arrangements around Mg (Table 11) completes the model of the cation redistribution during the diagenetic transformation of S to T layers. As in the case of Fe^{2+}, the local cation arrangement around divalent Mg consisting of three trivalent cations is the most stable. Significant increase of the 3Al arrangements most probably is related to degradation of 2AlMg arrangements. Indeed, decreasing w_i values for the arrangements 2AlMg (Table 11) including automatically $\boldsymbol{b_1}$- or $\boldsymbol{b_2}$-oriented Mg-Mg pairs in unclustered areas of the cation

distributions imply that Mg release occurs at the expense of the arrangements that are unfavorable with respect to homogeneous dispersion of octahedral charge. (The decreasing b_1- or b_2-oriented pairs are in Figs. 6b and 6d for highly transformed samples.) Then, the decreasing arrangements may be a result of Mg release both in unclustered areas and in the ordered clusters. Decreasing w_i values for the arrangements $2AlFe^{3+}$ are most probably also related to their transformation into the 3Al configurations due to replacement of Fe^{3+} for Al (Table 11).

For the Cambrian and Jurassic shales, the transformation of S to T layers occurs through a solid-state tetrahedral Al for Si substitution and subsequent fixation of NH_4 in interlayers (Lindgreen et al. 1991, 2000; Drits et al. 1997b, 2002). The present investigation of short-range cation order and composition of the clusters in the octahedral sheet where Al substitutes for Mg and Fe at cluster edges is also only compatible with a solid-state transformation for these I-S(-V) phases in shale.

ACKNOWLEDGMENTS

The authors gratefully acknowledge D. Dyar for valuable comments and suggestions. This research was supported by the Russian Science Foundation (grant 05-05-64135).

REFERENCES CITED

Anderson, J.U. (1963) An improved pretreatment for mineralogical analysis of samples containing organic matter. Clays and Clay Minerals, 10, 380–388.

Bancroft, G.M. (1974) Mőssbauer spectroscopy, 252 p. MacGraw Hill, New York.

Besson, G. and Drits, V.A. (1997a) Refined relationships between chemical composition of dioctahedral fine-dispersed mica minerals and their infrared spectra in the OH-stretching region. Part 1. Identification of the stretching bands. Clays and Clay Minerals, 45, 158–169.

——— (1997b) Refined relationships between chemical composition of dioctahedral fine-dispersed mica minerals and their infrared spectra in the OH-stretching region. Part 2. The main factors affecting OH-vibrations and quantitative analysis. Clays and Clay Minerals, 45, 170–183.

Besson, G., Bookin, A.S., Dainyak, L.G., Rautureau, M., Tsipursky, S.I., Tchoubar, C, and Drits, V.A. (1983) Use of diffraction and Mössbauer methods for the structural and crystallochemical characterization of nontronites. Journal of Applied Crystallography, 16, 374–383.

Bookin, A.S., Dainyak, L.G., and Drits, V.A. (1978) Interpretation of the Mössbauer spectra of layer silicates on the basis of structural modelling. Physics and Chemistry of Minerals, 3, 58–59.

Coey, J.M.D. (1980) Clay Minerals and their transformations studied with nuclear techniques: The contribution of Mössbauer spectroscopy. Atomic Energy Review, 18, 73–124.

Cuadros, J. (2002) Structural insights from the study of Cs-smectites submitted to wetting- and drying cycles. Clay Minerals, 37, 471–486.

Cuadros, J. and Altaner, S.P. (1998) Compositional and structural features of the octahedral sheet in mixed-layer illite-smectite from bentonites. European Journal of Mineralogy, 10, 111–124.

Cuadros, J., Sainz-Diaz, C.I., Ramirez, R., and Hernandez-Laguna, A. (1999) Analysis of Fe segregation in the octahedral sheet of bentonitic illite-smectite by means of FTIR, ^{27}Al MAS NMR and reverse Monte Carlo simulations. American Journal of Science, 299, 293–308.

Dainyak, L.G. (1980) Interpretation of Mössbauer spectra of Fe^{3+}-bearing layer silicates on the base of structural modelling. Ph.D. thesis, Geological Institute, Academy of Sciences of USSR, Moscow (in Russian).

Dainyak, L.G. and Drits, V.A. (1987) Interpretation of Mössbauer spectra of nontronite, celadonite, and glauconite. Clays and Clay Minerals, 35, 363–372.

Dainyak, L.G. and Kheifits, L.M. (1999) The improved equation for the Fe^{3+} quadrupole doublet assignment and computer simulation of cation distribution in trans-vacant dioctahedral micas. P. 72 in: EUROCLAY 1999 program with Abstracts. Institute of Geological Sciences PAN, Krakow, 176 pp.

Dainyak, L.G., Bookin, A.S., Drits, V.A., and Tsipursky, S.I. (1981) Mössbauer and electron diffraction study of cation distribution in celadonite. Acta Crystallographica, A-37 (suppl.), C-362.

Dainyak, L.G., Drits, V.A, and Heifits, L.M. (1992) Computer simulation of cation distribution in dioctahedral 2:1 layer silicates using IR-data: Application to Mössbauer spectroscopy of a glauconite sample. Clays and Clay Minerals, 40, 470–479.

Dainyak, L.G., Drits, V.A., and Lindgreen, H. (2004) Computer simulation of octahedral cation distribution and interpretation of the Mössbauer Fe^{2+} components in dioctahedral trans-vacant micas. European Journal of Mineralogy, 16, 451–468.

Drits, V.A. (1975): Structural and crystal chemical peculiarities of layer silicates. In A.G. Kossovskaya, Ed., Crystal Chemistry of Minerals and Problems of Geology, p. 35–51. Nauka, Moscow (in Russian).

Drits, V.A., Dainyak, L.G., Muller, F., Besson, G., and Manceau, A. (1997a) Isomorphous cation distribution in celadonites, glauconites and Fe-illites determined by Infrared, Mössbauer and EXAFS spectroscopy. Clay Minerals, 32, 153–180.

Drits, V.A., Sakharov, B.A., Lindgreen, H., and Salyn, A.L. (1997b) Sequential structure transformation of illite-smectite-vermiculite during diagenesis of Upper Jurassic shales from the North Sea and Denmark. Clay Minerals, 32, 351–371.

Drits, V.A., Sakharov, B.A., Dainyak, L.G., Salyn, A.L, and Lindgreen, H. (2002) Structural and chemical heterogeneity of illite-smectites from Upper Jurrasic mudstones of East Greenland related to volcanic and weathered parent rocks. American Mineralogist, 87, 1590–1607.

Drits, V.A., Lindgreen, H., Sakharov, B.A., Jakobsen, H.J., and Zviagina, B.B. (2004) The detailed structure and origin of clay minerals at the Cretaceous/Tertiary boundary, Stevns Klint (Denmark). Clay Minerals, 39, 367–390.

Eslinger, E., Highsmith, P., Albers, D., and deMayo, B. (1979) Role of iron reduction in the conversion of smectite to illite in bentonites in the disturbed belt, Montana. Clays and Clay Minerals, 27, 327–338.

Goodman, B.A. (1976): The effect of lattice substitutions on derivation of quantitative site populations from the Mössbauer spectra of 2:1 layer lattice silicates. Journal de Physique, 37, C6-819–823.

Gunnlaugsson, H.P. (1999) Vinda-Excell utility for analysis of Mössbauer spectra. http://www.ifa.au.dk/~hpg/vinda.htm.

Hansen, P.L. and Lindgreen, H. (1989) Mixed-layer illite/smectite diagenesis in Upper Jurassic claystones from the North Sea and onshore Denmark. Clay Minerals, 24, 197–213.

Hower, J., Eslinger, E.V., Hower, M.E., and Perry, E.A. (1976) Mechanism of burial metamorphism of argillaceous sediments. Geological Society America Bulletin, 87, 725–737.

Lindgreen, H. (1994): Ammonium fixation during illite-smectite diagenesis in Upper Jurassic shale, North Sea. Clay Minerals, 29, 527–537.

Lindgreen, H., Jacobsen, H., and Jakobsen, H.J. (1991) Diagenetic structural transformations in North Sea Jurassic illite/smectite. Clays and Clay Minerals, 39, 54–69.

Lindgreen, H., Drits, V.A., Sakharov, B.A., Salyn, A.L., Wrang, P., and Dainyak, L.G. (2000) Illite-smectite structural changes during metamorphism in black Cambrian Alum shales from the Baltic area. American Mineralogist, 85, 1223–1238.

Lottermoser, W., Kaliba P., Forcher K., and Amthauer, G. (1993) A computer program for the evaluation of Mössbauer data. Unpublished. University of Salzburg, Austria.

Lougear, A., Grodzicki, M., Bertoldi, C., Trautwein, A.X., Steiner, K., and Amthauer, G. (2000) Mössbauer and molecular orbital study of chlorites. Physics and Chemistry of Minerals, 27, 258–269.

Madejova, J., Putyera, K., and Čičel, B. (1992) Proportion of central atoms in octahedral layers of smectites calculated from IR spectra. Geologica Carpathica Series Clays, 43, 117–120.

Madejova, J., Komadel, P., and Čičel, B. (1994) Infrared study of octahedral site populations in smectites. Clay Minerals, 29, 319–326.

Manceau, A., Lanson, B., Drits, V.A., Chateigner, D., Gates, W.P., Wu, J., Huo, D., and Stucki, J.W. (2001) Oxidation-reduction mechanism of iron in dioctahedral smectites. I. Crystal chemistry of oxidized reference nontronites. American Mineralogist, 85, 133–152.

McCarty, D., Drits, V.A., Sakharov, B.A., Zviagina, B.B., Ruffel, A., and Wach, G. (2004) Heterogeneous mixed-layer clays from the Cretaceous Greensand-Isle of Wight, Southern England. Clays and Clay Minerals, 52, 552–575.

Mehra, O.P. and Jackson, M.L. (1960) Iron oxide removal from soils and clays by a dithionite citrate system buffered with sodium bicarbonate. Clays and Clay Minerals, Proceedings 7th National Conference, Washington, D.C., 1958, 317–327.

Méring, J. and Glaeser, R. (1954) Sur la role de la valence des cations échangeables dans la montmorillonite. Bulletin de la Société Française de Minéralogie et Cristallographie, 77, 519–530.

Muller, F., Besson, G., Manceau, A., and Drits, V.A. (1997) Distribution of isomorphous cations within octahedral sheets in montmorillonite from Camp-Bertaux. Physics and Chemistry of Minerals, 24, 159–166.

Nadeau, P. and Bain, D. (1986) Composition of some smectites and diagenetic illitic clays and implications for their origin. Clays and Clay Minerals, 34, 455–464.

Perry, E.A. and Hower, J. (1970) Burial diagenesis in Gulf Coast pelitic sediments. Clays and Clay Minerals, 18, 165–177.

Rancourt, D.G. (1994) Mössbauer spectroscopy of minerals. II. Problem of resolv-

ing *cis* and *trans* octahedral Fe^{2+} sites. Physics and Chemistry of Minerals, 21, 250–257.
Rancourt, D.G. and Ping, J.Y. (1991) Voigt-based methods for arbitrary-shape static hyperfine parameters distributions in Mössbauer spectroscopy. Nuclear Instruments and Methods in Physics Research, B58, 85–97.
Rancourt, D.G., Ping, J.Y., Boukili, B., and Robert, J.L. (1996) Octahedral-site Fe^{2+} quadrupole splitting distributions from Mössbauer spectroscopy along the (OH,F)-annite join. Physics and Chemistry of Minerals, 23, 63–71.
Redhammer, G.J. (1998) Characterisation of synthetic trioctahedral micas by Mössbauer spectroscopy. Hyperfine Interactions, 117, 85–115.
Redhammer, G.J., Beran, A., Schneider, J., Amthauer, G., and Lottermoser, W. (2000) Spectroscopic and structural properties of synthetic micas on the annite-siderophyllite binary: Synthesis, crystal structure refinement, Mössbauer, and infrared spectroscopy. American Mineralogist, 85, 449–465.
Redhammer, G.J., Amthauer, G., Lottermoser, W., and Roth, G. (2002) Quadrupole splitting distribution of Fe^{2+} in synthetic trioctahedral micas. Hyperfine interactions, 141/142, 345–349.
Rusakov, V.S. (1999) Reconstruction of the hyperfine parameters distributions for Mössbauer spectra of locally inhomogeneous systems. Bulletin Russian Academy of Science Physics, 7, 1093–1098.
Rusakov, V.S. and Chistyakova, N.I. (1992) Mössbauer Program Complex MSTools. Latin American Conference on Applications of the Mössbauer Effect, LACAME'92. Buenos Aires, Argentina, 7, 3.
Sainz-Diaz, C.I., Caudros, J., and Hernandez-Laguna, A. (2001a) Analysis of cation distribution in the octahedral sheet of dioctahedral 2:1 phyllosilicates by using inverse Monte Carlo methods. Physics and Chemistry of Minerals, 28, 445–454.
Sainz-Diaz, C.I., Hernandez-Laguna, A., and Dove, M.T. (2001b) Modeling of dioctahedral 2:1 phyllosilicates by means of transferable empirical potentials. Physics and Chemistry of Minerals, 28, 130–141.
Sainz-Diaz, C.I., Timon, V., Botella, V., Artacho, E., and Hernandez-Laguna, A. (2002) Quantum-mechanical calculations of dioctahedral 2:1 phyllosilicates: Effect of octahedral cation distribution in pyrophyllite, illite, and smectite. American Mineralogist, 87, 958–965.
Sainz-Diaz, C.I., Palin, E.J., Dove, M.T., and Hernandez-Laguna, A. (2003a) Monte Carlo simulations of ordering of Al, Fe and Mg cations in the octahedral sheet of smectites and illites. American Mineralogist, 88, 1033–1045.
Sainz-Diaz, C.I., Palin, E.J., Hernandez-Laguna, A., and Dove, M.T. (2003b) Octahedral cation ordering of illite and smectite. Theoretical exchange potential determination and Monte Carlo simulation. Physics and Chemistry of Minerals, 30, 382–392.
Sakharov, B.A., Besson, G., Drits, V.A., Kameneva, M.Y., Salyn, A.L., and Smoliar, B.B. (1990) X-ray study of the nature of stacking faults in the structure of glauconites. Clay Minerals, 25, 419–435.
Shabani, A.A.T., Rancourt, D.G., and Lalonde, A.E. (1998) Determination of *cis* and *trans* Fe^{2+} populations in $2M_1$ muscovite by Mössbauer spectroscopy. Hyperfine Interactions, 117, 117–129.
Shutov, V.D., Drits, V.A., and Sakharov, B.A. (1969a) On the mechanism of a postsedimentary transformation of montmorillonite into hydromica. In L. Heller, Ed., Proceedings International Clay Conference, Tokyo, 1969, 1, p. 523–532. Jerusalem University.
Shutov, V.D., Drits, V.A., and Sakharov, B.A. (1969b) On the mechanism of a postsedimentary transformation of montmorillonite into hydromica: Discussion. In L. Heller, Ed., Proceedings International Clay Conference, Tokyo, 1969, 2, p. 126–129. Jerusalem University.
Slonimskaya, M.V., Besson, G., Daynyak, L.G., Tchoubar, C., and Drits, V.A. (1986) The interpretation of the IR spectra of celadonites and glauconites in the region of OH-stretching frequencies. Clay Minerals, 21, 377–388.
Smoliar-Zviagina, B.B. (1993) Relationships between structural parameters and chemical composition of micas. Clay Minerals, 28, 603–624.
Środoń, J., Elsass, F., McHardy, W.J., and Morgan, D.J. (1992) Chemistry of illite-smectite inferred from TEM measurements of fundamental particles. Clay Minerals, 27, 137–158.
Timon, V., Sainz-Diaz, C.I., Botella, V., and Hernandez-Laguna, A. (2003) Isomorphous cation substitution in dioctahedral phyllosilicates by means of ab initio quantum mechanical calculations on clusters. American Mineralogist, 88, 1788–1795.
Tsipursky, S.I., Drits, V.A., and Chekin, S.S. (1978): Study of structural ordering of nontronite by oblique texture electron diffraction. Izvestiya Akademii Nauk S.S.S.R., Seriya Geologicheskaya, 10, 105–113 (in Russian).
Wivel, C. and Mørup, S. (1981): Improved computational procedure for evaluation of overlapping hyperfine parameter distributions in Mössbauer spectra. Journal of Physics E: Scientific Instruments, 14, 605–610.
Zviagina, B.B. (2004) Interpretation of IR spectra of mixed-layer illite-smectites and illite tobelite-smectites in the region of OH-stretching vibrations. Proceedings of the 5th European Conference on Mineralogy and Spectroscopy, September 2004, Vienna, Austria. Mitteilungen der Österreichischen Mineralogischen Gesellschaft, 149.
Zviagina, B.B., McCarty, D.K., Środoń, J., and Drits, V.A. (2002) Interpretation of IR spectra of dioctahedral 2:1 phyllosilicates in the region of OH-stretching vibrations. Proceedings of the 18th General Meeting of the International Mineralogical Association, September 2002, Edinburg, Scotland, 158.
——— (2004) Interpretation of IR spectra of dioctahedral smectites in the region of OH-stretching vibrations. Clays and Clay Minerals, 52, 399–410.

Manuscript received July 29, 2005
Manuscript accepted October 19, 2005
Manuscript handled by Stephen Guggenheim

Appendix 1

To compare the model approach and QSD analysis using the same spectrum, D. Dyar (private communication) evaluated the spectrum of the Fe^{3+}-rich illite 60 using QSD analysis as implemented in the laboratory of Eddy DeGrave, University of Gent (see Wivel and Mørup 1981). This sample was studied previously in detail by Dainyak et al. (2004) and its spectrum was fitted in the model approach. Dyar obtained two doublets corresponding to Fe^{3+}, as in the model approach, with close values for quadrupole splittings and isomer shifts and two doublets of Fe^{2+} instead of three (Appendix Table 1). Although the QSD fit to the spectrum resulted in a greater χ-squared value (2.6) than ours (1.07), probably due to the lower number of doublets, the fitted parameters were suitable to apply the model methodology.

Several simulation program cycles using different groupings, which correspond to QSD-fitted S_j^n, and IR data for sample 60 (Dainyak et al. 2004) were sufficient to obtain the cation distribution satisfying the QSD-fitted parameters. Appendix Table 2 shows the cation distribution simulation results as the individual occurrence probabilities obtained using the preset grouping (indicated by underlines), w_i, and comparison of the total occurrence probabilities, $W_j = \Sigma_i w_i$, for the groups and calculated quadrupole splittings, $\Delta_j^{calc} = \Sigma_i \Delta_i^{pred(tent)} \cdot w_i^n$, with the relative doublet intensities, S_j^n, and corresponding quadrupole splittings, Δ_j^{fit}. In addition, Appendix Table 2 contains predicted and tentative individual quadrupole splittings with the corresponding local cation arrangements for Fe^{3+} and Fe^{2+}. As it follows from the good agreement between the calculated and fitted parameters, the computer program finds acceptable cation distribution reconstructions for the QSD-fitted parameters.

It is important that the two cation distributions display similar features. Indeed, the main contribution to the inner doublet Fe^{3+} is due to the arrangement $2AlFe^{3+}$ whereas the arrangements $2AlFe^{2+}$ and 2AlMg prevail as the contributors to the doublet Fe^{3+} with the greater Δ_j^{fit} [Fig. 5 and Table 6 in Dainyak et al. (2004) for the model approach and Appendix Table 2 for the QSD fitting.] Relative contributions w_i^n into relative intensities S_j^n remain nearly the same. However, the relationship among these three basic arrangements in the reconstructed cation distribution changes according to the difference between S_j in the

Appendix Table 1. Mössbauer (fitted) parameters

	Fe^{3+}				Fe^{2+}				
Doublet	δ_j	Δ_j	Γ	S^n_j	δ_j	Δ_j	Γ	S^n_j	χ^2
Dainyak et al. 2004*									
1	0.35	0.46	0.39	0.45	1.12	2.49	0.58	0.39	
2	0.35	0.86	0.87	0.55	1.14	2.84	0.30	0.33	
3					1.13	2.96	0.24	0.28	1.07
Dyar 2005									
1	0.345	0.499	0.444	0.645	1.12	2.641	0.443	0.51	
2	0.401	1.011	0.954	0.355	1.131	2.932	0.233	0.49	2.606

* Pseudo-Voigt line shape was used in the model fitting.

model approach and QSD fitting. The same occurs for the partial spectra Fe^{2+}. Unlike the QSD fitting, the model fitting includes three Fe^{2+} doublets. The two inner doublets are provided by the arrangements $2AlFe^{3+}$ and 3Al, respectively, whose occurrence probabilities are approximately equal (see Table 7 in Dainyak et al. 2004). The inner doublet of the QSD fitting, which is stipulated by these arrangements also having close occurrence probabilities, may be considered as a doublet averaged over the inner doublets of the model fitting.

Appendix Figure 1 shows a portion of the cation distribution reconstruction obtained on the basis of the QSD-fitted Mössbauer parameters. This pattern reproduces the basic features of the cation distribution reconstruction reported in Dainyak et al. (2004): no preference of R^{2+} to one of the two *cis*-positions; moderate clustering, that is, Al-matrix is rather diluted by clusters of mixed composition (Al, Mg, Fe^{2+}); "in spite of the lack of any site preference for R^{2+}, the clusters of mixed composition are characterized by groupings having R^{3+} cations surrounded by R^{2+} cations and vice versa prevailing." (Dainyak et al. 2004, p. 465). The change in the occurrence probabilities for the main cation arrangements in the cation distribution reconstruction based on the QSD fitted parameters may imply some changes in the size of clusters of mixed composition. However, in spite of certain variations in proportions of Fe^{2+} and Mg in clusters, the described peculiarities of the cation distributions will be preserved because so will the total content of R^{2+} cations participating in clustering.

Thus, the general features in the two cation distributions are similar although there may be certain differences in the details. The question therefore is to what extent is it reasonable and, more importantly, possible to refine the data on clustering peculiarities? In other words, to what extent are these fine differences in the details of cation distributions meaningful, considering that both cation distribution reconstructions agree equally well with the IR and XRD data? Considering that the problem of Mössbauer spectra refinement is mathematically incorrect in that a spectrum can be fitted in different ways with acceptable statistical parameters, it seems that the two cation distributions (which are actually two interpretations) can be regarded equally valid. When studying a single sample, it does not seem feasible to decide which cation distribution is closer to the actual structure as regards the fine details, such as subtle differences in clustering characterization. It may be possible to solve such a problem by studying a series of samples and employing the data of additional physical methods.

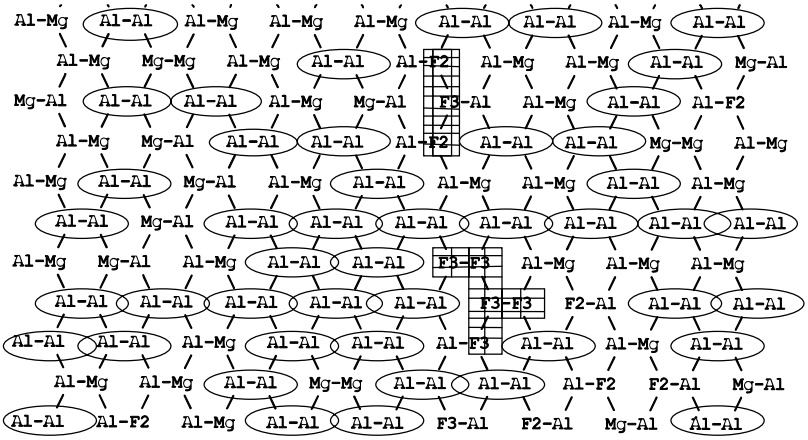

APPENDIX FIGURE 1. Cation distribution reconstruction for sample 60 by the QSD-fitted Mössbauer parameters.

APPENDIX TABLE 2. The results for the cation distribution reconstructed by the QSD-fitted parameters for sample 60

		Fe^{3+}						Fe^{2+}				
Arrangement	Δ_i^{pred} mm/s	w_i	W_i	S_j^n	Δ_j^{calc} mm/s	Δ_j^{fit} mm/s	Δ_i^{tent} mm/s	w_i	W_j	S_j^n	Δ_j^{calc} mm/s	Δ_j^{fit} mm/s
$3Fe^{2+}$	0.						1.2					
$2Fe^{2+}Mg$	0.13						1.4					
$3Fe^{3+}$	0.17	0.003					1.61					
$2MgFe^{2+}$	0.26						1.7					
$2Fe^{3+}Al$	0.33	0.085					1.85					
$2Fe^{2+}Fe^{3+}$	0.34	0.012					1.87					
3Mg	0.39						1.90					
$MgFe^{2+}Fe^{3+}$	0.48	0.033					2.10					
$2Fe^{2+}Al$	0.49	0.036					2.30					
$2AlFe^{3+}$	0.51	0.467	0.624	0.645	0.48	0.499	2.49	0.233				
$2MgFe^{3+}$	0.61	0.003					2.60					
$AlMgFe^{2+}$	0.63	0.064					2.66					
$2Fe^{3+}Fe^{2+}$	0.65						2.75					
3Al	0.74	0.067					2.84	0.267				
2MgAl	0.78	0.015					2.85	0.002				
$2Fe^{3+}Mg$	0.79						2.87					
$AlFe^{2+}Fe^{3+}$	0.86	0.012					2.87					
$AlMgFe^{3+}$	1.02	0.009					2.87		0.502	0.49	2.68	2.641
$2AlFe^{2+}$	1.06	0.109					2.90	0.148				
2AlMg	1.40	0.097	0.376	0.355	0.994	1.011	2.96	0.35	0.498	0.51	2.94	2.932